Durham E-Theses

Diffraction and Solid State NMR Studies of Inorganic Framework Materials.

Yue, Rebecca Katherine Karbo

How to cite:

Use policy

Diffraction and Solid State NMR Studies of Inorganic Framework Materials

A thesis submitted for the requirements for the degree of Master of Philosophy

Rebecca Yue MChem

Supervisors: Prof. John S.O. Evans & Dr. Paul Hodgkinson

Department of Chemistry, University of Durham

2012

Abstract

Framework materials with the formula AM_2O_7 and AM_2O_8 are of great interest and have been shown to exhibit negative thermal expansion (NTE) and interesting oxygen dynamics. Solid-state NMR was used to probe the local environment of the nuclei, which often complements information obtained from diffraction based techniques. *Ab initio* calculations were also used and compared to experimental spectra.

Cubic-$ZrMo_2O_8$ is of particular interest due as it has been shown to exhibit NTE over a wide temperature range (0-1020 K). In this report we have characterised various phases of $ZrMo_2O_8$ using variable temperature powder X-ray diffraction, SEM and ^{17}O NMR. We have shown that the particle size of the precursor determines whether the cubic phase can be made purely.

$RbNbOP_2O_7$ exhibits 2 reversible phase transitions occur at 346 K and 276 K. The data suggests the first phase transition on warming changes from low to high symmetry, followed by a second phase transition from high to low symmetry to a structure similar to the low temperature structure. However, the intermediate phase has not yet been characterised and NMR has been employed to help complement other diffraction methods. ^{31}P 1D NMR and ^{97}Nb echo experiments showed little difference in the NMR spectra obtained at different temperatures. However, much larger changes have been observed in ^{87}Rb echo NMR performed on a 400 MHz spectrometer and the 850 MHz National Facility spectrometer. The data shows the intermediate phase structure is related to the low temperature phase.

$SnMo_2O_8$ differs in its behaviour compared to other members of AM_2O_8 family, in that it exhibits positive thermal expansion with a phase transition at approximately 300 K. In this case, broad features that do not vary significantly with temperature, suggesting static disorder.

Acknowledgements

Firstly, I would like to thank both my supervisors, Paul Hodgkinson and John Evans for all their help and guidance throughout this whole process. Thank you for your support and understanding.

Simon Allen, Matt Hampson and Anne Soleilhavoup for the work they did for their PhD's which has been the building blocks for this thesis. Thank you so much David Apperley and Fraser Markwell for your help and use of the NMR service spectrometer and all other advice and help you have given me.

A real special thanks to Jenny Readman and Sarah Tallentire who I have collaborated with. It was so lovely to work with you and I cherish all the advice, help and guidance. Thank you so much. Leon in SEM you helped me and kept me company when I was doing my SEM. Thank you.

I would also like to thank Andy Ilott and Dave Burnell who kept me company (and sane) during my first year of research. I would also like to thank the members of all the research groups, Anuji, Ilya , Andrew and Julia. A special thanks to Emma who has listened, given advice and helped me no end throughout my time in Durham. I really couldn't have done it without you.

Lastly, I would like to thank my family, friends and love ones who have had to deal with every single emotion under the sun. Without your support I would have never finished this. Your unconditional love never waned and for that I am truly thankful.

Finally, like the old proverb says "what doesn't kill you makes you stronger".

Rebecca Yue
December 2012

"It does not matter how slowly you go so long as you do not stop"

Confucius

Declaration and Statement of Copyright

The work described in this thesis is entirely my own, except where I have acknowledged help from a named person or given a reference to a published source or thesis.

The research presented was performed ion the Department of Chemistry, University of Durham bewtween October 2009 and October 2012, the results of which have not been submitted for a degree in this or any other university. This thesis conforms to the word limit set out in the Degree Regulations of the university.

The copyright of this thesis rests with the author. No quotation should be published without their prior consent and information derived from it should be acknowledged in the form of a reference.

Glossary of Symbols and Abbreviations

AC Spectroscopy

CSA   Chemical Shift Anisotropy

CTE   Co-efficient of Thermal Exansivity

C_Q Quadrupolar Coupling Constant

δ_{iso} Absolute Chemical Shifts

DFT   Density Functional Theory

DOR   Double rotation

EFG   Electric Field Gradient

e.s.d.   estimated standard deviation

e_q Electric Quadrupolar Moment

EXSY   Exchange Spectroscopy

FID   Free Induction Decay

FT   Fourier Transform

FWHM   Full Width Half Maximum

GIPAW   Gauge Including Projector Augmented Wave

HF   Hartree Fock

I Spin Quantum Number

J coupling   Scalar Inter-Nuclear Coupling

LT   Low Temperature

MAS   Magic Angle Spinning

MQMAS   Multiple Quantum Magic Angle Spinning

NMR   Nuclear Magnetic Resonance

NTE   Negative Thermal Expansion

ppm   parts per million

PXRD   Powder X-ray Diffraction

RF   Radio Frequency

RUM   Rigid Unit Mode

SEM   Scanning Electron Miscroscopy

SCF   Self Consistent Fields

s/n   signal to noise ratio

SOFCs   Solid Oxide Fuel Cells

SSNMR   Solid State Nuclear Magnetic Resonance

T_1 Spin-lattice Relaxation Time

TOPAS TO Pattern Analysis Software

VT Variable Temperature

XRD X-ray Diffraction

QCPMG Quadrupolar Carr-Purcell Meiboom-Gill

Addendum

1.

Unlike [17]O, where there are extensive studies into *ab initio* calculated NMR values, there have been relatively few studies investigating the quadrupolar parameters of [93]Nb nuclei, and, to the best of our knowledge, no detailed studies for [87]Rb. For [93]Nb one explanation for this may be the lack of an adequate library of Nb[V] containing model compounds. It is, therefore, extremely difficult to characterise niobate systems, either with respect to chemical shift or quadrupolar parameters.

Lo et al. attempted to compare DFT calculated and experimentally acquired [93]Nb quadrupolar parameters[1] for Nb[I] and Nb[V] half-sandwiched cyclopentadieyl complexes. Restricted Hartree-Fock (RHF) and hybrid DFT (B3LYP) using Gaussian 03 calculations were used and produced reasonable correlated results with the experimental values. Hanna *et al.* realised that one of the problems that had previously affected precise correlations between calculated and experimental data was failing to account for second order (-1/2 ↔ 1/2) central transition shifts. Hanna *et al.* used variable B_0 field data to establish an accurate basis in which the NMR interaction parameters could be measured. A variety of niobate compounds was investigated and the experimental data was used and compared to calculated values. Several different computational methods were used, namely WIEN2K, NMR-CASTEP and Gaussian 03. Full geometry optimisations of the structures were needed before the calculation of the NMR interactions, as many of the structures used were only partially completed. It was shown that using WEIN2K and CASTEP showed either excellent or very good correlation with the experimentally measured values. However, when using Gaussian 03 the calculated values were not as accurate and had significantly weaker correlations with the experimental values.

Hanna *et al.*[2] also suggested that it was possible to distinguish between different perovskite polymorphs of $NaNbO_3$ using NMR and DFT calculations. Johnston *et al.*[3] investigated this suggestion further. Various polymorphs of $NaNbO_3$ were studied and NMR interactions calculated for all the compounds using NMR-CASTEP

using GIPAW and ultra-soft pseudo-potentials. Once geometry optimisation of all structures were completed, the NMR parameters for many of the pervoskite phases had similar values and thus it is not conclusive that *ab initio* calculations can be used to distinguish between these polymorphs.

2.

The ^{17}O MAS NMR undertaken in this work represents measurements undertaken at only one magnetic field strength (B_0 = 11.7 T). All of the reported ^{17}O resonances (and those from quadrupolar nuclei in general) will exhibit variation in the 'apparent' chemical shift with the external magnetic field strength. This variation can be explained by the relationship between the isotropic second-order shift and the magnetic field.Equation 1 gives the isotropic second-order shift as the position of the centre of gravity of the (static) powder pattern for zero quadrupolar asymmetry:

$$-\frac{3\chi^2}{10\nu_0}f(I)$$ **Equation 1**

Where χ is the quadrupolar coupling constant, ν_0 is the NMR frequency and *f(I)* is a spin-dependent factor. This equation shows clearly the inverse dependence on ν_0 (i.e. B_0). The centre of gravity of the central transition is invariant to spinning, so Equation 1 can explain both static and MAS isotropic shifts.

In this work all simulations of spectra included the quadrupolar interactions to second order, so the shift due to second-order isotropic shifts would be included. The chemical shift is always to lower frequency, *i.e.* a lower apparent chemical shift is observed. ^{17}O has *f(I)* value of 0.020 and the largest C_Q calculated in this work was 5 MHz. This corresponds to a 2 kHz shift to lower frequency for the ^{17}O peak. All the reported experimentally obtained shifts are obtained from the peak maximum and include the second-order isotropic shift. It is also important to note that both experimental and simulated spectra incorporate second order shift and hence comparisons between the two can be deduced.

3.

There are two alternative definitions, with differing symbols, to describe the shielding/chemical shift anisotropy.   In this thesis tables show chemical shift anisotropies (CSA) from calculated from the CASTEP magres file using the programme magres2pNMRsim. This programme uses the conventional definition of anisotropy, ζ, as defined in Equation 2:

$$\zeta = R_{ZZ} - R_{iso} \qquad \text{Equation 2}$$

Where R_{zz} is the principal Z component of the tensor and R_{iso} is the isotropic average which can be defined in Equation 3:

$$R_{iso} = \frac{1}{3}(R_{XX} + R_{YY} + R_{ZZ}) \qquad \text{Equation 3}$$

where R_{XX}, R_{YY} and R_{ZZ} are the principal components of the tensor. CASTEP uses the alternative definition of anisotropy, ΔR, defined in Equation 4:

$$\Delta R = R_{ZZ} - \frac{1}{2}(R_{XX} + R_{YY}) \qquad \text{Equation 4}$$

. The definitions are related by $\zeta = 2\Delta R/3$.

Chapter 1

The table below shows the Euler angles (α, β and γ) for the Rb and Nb NMR tensors in the high temperature and low temperature RbNbOP$_2$O$_7$ structures calculated by magres2pNMRsim from the CASTEP output.   These values were used when simulating the spectra in Figures 6.7 and 6.8.

Nucleus		Euler angles (α, β, γ)/ degrees	
		LT RbNbOP$_2$O$_7$	**HT RbNbOP$_2$O$_7$**
Rb	**Shift**	157.1, 33.41, 107.00	0, 97.55, 90.00
	Quadrupolar	136.1, 31.17, 65.68	180.00, 21.62, 90.00
Nb	**Shift**	45.22, 5.956, -56.39	-90.00, 6.56, 90
	Quadrupolar	55.99, 9.771, 117.4	-90, 16.71, 90

4.

There has not been much investigation into the pseudo-potentials of heavier nuclei such as Rb and Nb. When conducting the *ab initio* calculations there were several problems with the [87]Rb calculations regarding the pseudo-potentials and CASTEP calculation were unable to be performed. In order to try and rectify this issue, the configuration was adjusted slightly using a numerically stable pseudo-potential proposed by Keith Refson (Rutherford Appleton Laboratory). He suggested a new string configuration:

2 │2.5│2.5│1.8│5.9│7.4│8.9│40U2.2 : 50U+0U+0.125 : 41UU (qc=4.29) [ ]

It is important to note that while this pseudo-potential allows calculations to run it has not been rigorously tested. Furthermore, due to the lack of [93]Nb *ab initio* studies, one must also proceed with care when using these NMR parameters calculated in this work. More detailed investigation into the pseudo-potentials for heavier atoms is required. This may explain the differences in the calculated and experimentally obtained NMR parameter,in contrast to light elements such as ^{13}C where the pseudo-potentials have been extensively evaluated.

(1)   Lo, A. Y. H.; Bitterwolf, T. E.; Macdonald, C. L. B.; Schurko, R. W. *Journal of Physical Chemistry A* **2005**, *109*, 7073.

(2)   Hanna, J. V.; Pike, K. J.; Charpentier, T.; Kemp, T. F.; Smith, M. E.; Lucier, B. E. G.; Schurko, R. W.; Cahill, L. S. *Chemistry-a European Journal* **2010**, *16*, 3222.

(3)   Johnston, K. E.; Griffin, J. M.; Walton, R. I.; Dawson, D. M.; Lightfoot, P.; Ashbrook, S. E. *Physical Chemistry Chemical Physics* **2011**, *13*, 7565.

Chapter 2 Introduction and Literature review

Most materials show a positive coefficient of thermal expansion. This is due to increases in average bond lengths with increasing thermal energy. However, some materials show the opposite effect where a number of phenomena outweigh the general increase in bond length and hence show a negative coefficient of thermal expansion. In recent years negative thermal expansion (NTE) materials have been of particular interest. There are a number of potential applications these materials can be used for such as in low temperature sensing. Framework materials with the formula AM_2O_7 and AM_2O_8 (where A = Si, Ti, Ge, Sn; M = P, V for AM_2O_7 and A = Zr, Hf; M = W, Mo for AM_2O_8) have been shown to exhibit NTE and are of particular interest. In this work studies on $ZrMo_2O_8$, $SnMo_2O_8$ and $RbNbOP_2O_7$ have been carried out.

2.1 Classical ideas of thermal expansion

The simple harmonic oscillator can use used to demonstrate the bonding in simple diatomic molecules, such as HCl, in terms of vibrational motion. This assumes when a system is displaced from its equilibrium position it experiences a restoring force proportional to the displacement, illustrated by a parabolic potential energy curve (Figure 2.1). An analogy for this is to relate the movement in a covalent bond to that of the movement in a spring where movement of atoms is restricted to one dimension.
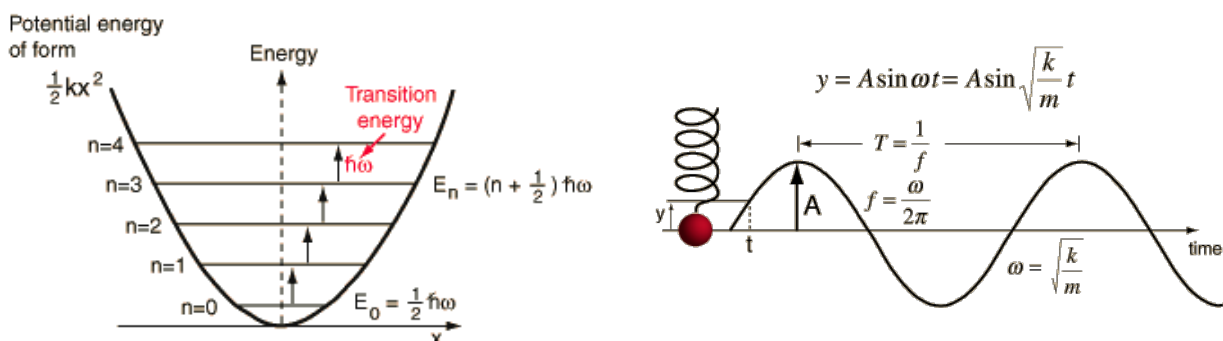
Figure 2.1 Parabolic potential energy curve illustrating simple harmonic motion in a simple diatomic molecule (left). Simple harmonic motion represented by the motion of mass on spring when experiencing elastic restoring force (Hooke's law) (right).[1]

The energy levels are quantised due to the boundary conditions which states that the system will not be found with infinitely large compressions or extensions. Boundary conditions also state the only permitted energy levels are:

$$E_v = \left(v + \frac{1}{2}\right)\hbar\omega$$

Equation 2.1

Where v= 0, 1, 2, 3 etc and:

$$\omega = \left(\frac{k}{m}\right)^{\frac{1}{2}}$$

Equation 2.2

The energy levels are equally spaced by $\hbar\omega$:

$$E_{v+1} - E_v = \hbar\omega$$

Equation 2.3

For objects with large mass, *i.e.* on the macroscopic scale, $\hbar\omega$ is negligible,. However, $\hbar\omega$ is of great importance for objects with masses similar to that of atoms. When the temperature is greater than 0 K, higher energy levels are populated according to the Boltzmann distribution. As such when $v = 0$ in the form of equation 1 the ground state energy is non-zero and the particles move in the equilibrium position.

$$E_0 = \frac{1}{2}\hbar\omega$$

Equation 2.4

The width of the potential energy curve is proportional to the amplitude of thermal vibrations for an atom. As the potential energy curve is symmetric, there is no shift in the equilibrium position as temperature increases and higher energy levels are populated. The coefficient of thermal expansivity, α, is zero for symmetric energy wells.

For real systems the inter-atomic potential is not symmetric and bonds are easier to extend than compress. A better approximation for the potential energy of a diatomic molecule is the Morse potential, where the motion becomes anharmonic as the restoring force is no longer proportional to the displacement as shown in Figure 2.2. The energy levels becomes less widely spaced at high excitations rather than staying uniformly spearated. At small displacements the Morse potential and harmonic oscilator potentials are similar, and the bond lengths increase slightly. At

increasing energy the displacements become larger and the bond lengths become increasing large and positive thermal expansion occurs. The rate of change of the potential energy curve is lower for the lengthening of bond lengths than shortening with increased energy. Stronger bonds have steeper and narrower potential energy wells as shown by r_1 and E_1 resulting in slower rate of increase in inter-atomic distance. This means smaller value of the co-efficient of thermal expansivity, α.
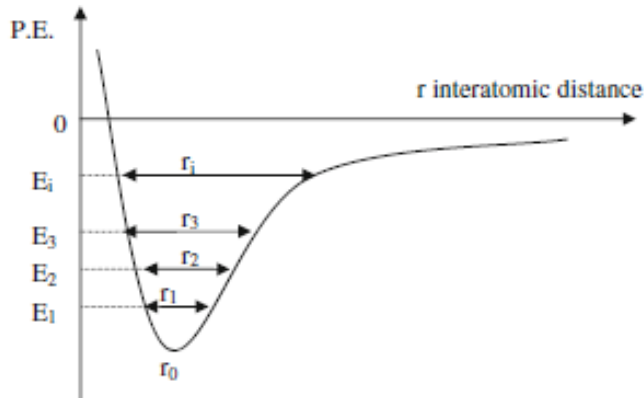
Figure 2.2 Graph of a general anharmonic potential energy well, illustrating a better approximation for the potential energy in a diatomic molecule. E_i and r_i is the energy ande interatomic distance respectively.[2]

2.2 Origin of negative thermal expansion

Negative thermal expansion (NTE) is in conflict with the basic principle of positive CTE for chemical bonds. Figure 2.2 only describes the bonding in a typical diatomic molecule (an individual bond). However, for more complicated systems this representation does not capture all the interactions present. In framework systems, strong inter-atomic forces are present via chemical bonds. If one atom moves away from equilibrium all closely linked atoms will be affected in a wave-like motion. This leads to the concept of phonons in extended materials.

Co-efficient of thermal expansivity (CTE) can be described in terms of volumetric, α_V, or linear, α_l terms:

$$\alpha_V = \frac{\Delta V}{V_0 \Delta T}$$

Equation 2.5

$$\alpha_L = \frac{\Delta L}{L_0 \Delta T}$$

Equation 2.6

Where ΔV and ΔL are the changes in volume and length respectively, V_0 and L_0 are the initial volume and length and ΔT is the change in temperature. In isotropic solids, Equations 1.5 and 1.6 are related by $\alpha_v = 3\,\alpha_l$, although in anisotropic solids, the relationship is not as simple as α_v is made up of α_a, α_b and α_c.

A material can be classified as a NTE material if a negative volume change occurs with increasing temperature, i.e. negative α. It is a temperature dependent function and it is important to state the temperature range in which the quotes co-efficient applies. NTE can arise in extended frameworks structural mechanisms dominating over CTE.

2.3 Mechanisms of NTE

Transverse vibrations

A phonon can be described as a quantum of excitation, a quantised mode of vibration, and can have a range of wavelengths, frequencies and amplitudes. Transverse and longitudinal modes are two important types of phonons. Transverse vibrational modes is one of the processes that can lead to NTE. Figure 1.3 shows the schematic diagram for a two-coordinate M-O-M linkage (M = metal, O = bridging oxygen) in a molecule and in a lattice. The longitudinal vibrational mode, *i.e.* along the M-O-M bond, tends to increase the bond length as temperature increases. The M-O bonds stretch and thus the M....M distance increases. The M-O bond lengths are relatively unchanged in transverse vibrational modes as the motion bends the linear linkages away from 180 $^{\circ}$ and decreases the effective M....M distance. This can lead to a net bulk volume contraction for a material. This mechanism generally dominates at low temperatures due to the lower excitation energy in transverse vibrational modes than longitudinal vibrational modes.
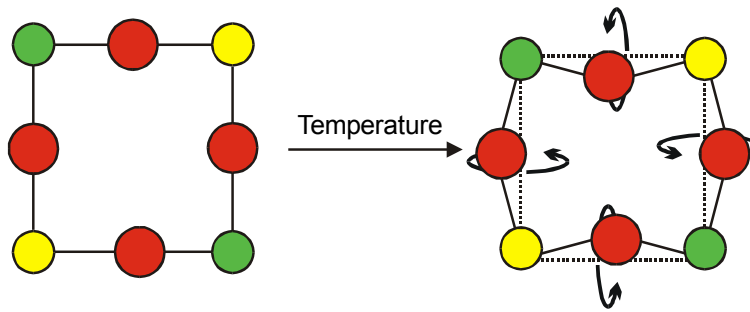
Figure 2.3 Schematic representation of transverse vibrations on a series of M-O-M bonds (O atoms represented in red, M atoms represented by yellow and green). The dashed line shows that in a transverse vibration, the bond length decreases and therefore the volume of the lattice decreases.[3]

The anharmonicity in extended solids can be quantified by the Grüneisen parameter, γ, and can be related to the volume (V), specific heat at a constant volume (C_v) and isothermal compressibility (K) by Equation 1.7.

$$\gamma = \frac{\alpha_v V}{K C_V}$$

Equation 2.7

When the vibrational mode frequency, v, decreases with volume, V, of the material, the Grüneisen parameter will lead to a negative contribution to the overall thermal expansion, α. Typical values of γ are in the range of 1 to 3.

$$\gamma = \frac{-d(lnv)}{d(lnV)}$$

Equation 2.8

Rigid Unit Modes (RUMs)

Some materials, such as quartz, show NTE at high temperatures, where the α-β phase transition occurs at 846 K. This cannot be explained by low frequency transverse vibrational modes. In framework materials, relatively stiff individual tetrahedra or octahedra with strong M-O bonds and relatively short O-O bonds prevent distortions of the individual polyhedra. The flexible 'hinges' of M-O-M or M-O-M' (M and M' = metal cations) have lower frequency phonon modes compared to the polyhedra and bending or rotation of these linkages is much more favourable

than the distortion of the polyhedra. The rotation of the M-O-M or M-O-M' linkages is due to the Grüneisen parameter.

Rigid unit modes is the term given to describe this transverse vibrational mode. RUMs can propagate through the framework structure with no distortion of the tetrahedra or octahedra, which rotate and translate as rigid units. They are low energy distortions and therefore low energy vibrational modes of the structure. RUMs were first decribed Megaw[4] and further investigations into these modes have been carried out by Dove, Heine *et al.*[5,6]

The lower the vibrational frequency, the more the thermal co-efficient will be affected. Excitation of RUMs and the "Folding up" of the structure will lead to the population of these vibrational modes and lead to NTE. This is analogous to the transverse vibrational modes as described in 0 and is shown schematically in figure below.
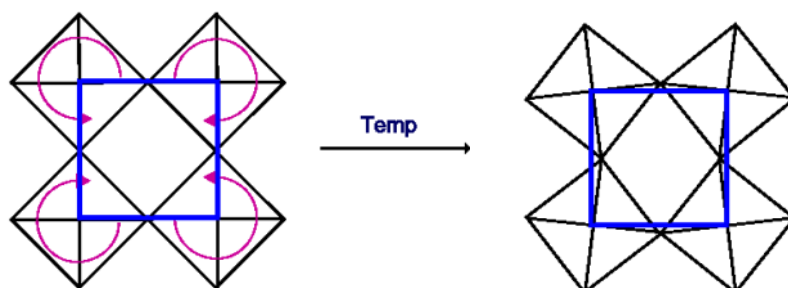
Figure 2.4 2D schematic representation of the contraction of a framework by coupled rotation in corner sharing polyhedral.[7]

2.4 NTE materials

Some framework materials with the formula AM_2O_8 are extended solids made up of corner-sharing polyhedral: octahedrally coordinated A^{4+} cations and tetrahedrally coordinated M^{6+} cations. The polyhedra are joined together by the shared vertices. The most studied AM_2O_8 phase is ZrW_2O_8, however in this project $ZrMo_2O_8$ and $SnMo_2O_8$ were studied.

ZrW_2O_8

During the 1960s[8,9] Zirconium tungstate was first observed but since the mid-1990s has the materials structure and properties attracted much interest[10-12]. The room temperature structure, α-ZrW_2O_8, was solved and refined in the space group $P2_13$ (a = 9.1575 Å). The structure (Figure 2.5) can be described in the same way as NaCl with Zr^{4+} cations and $W_2O_8^{4-}$ anions on a cubic lattice.
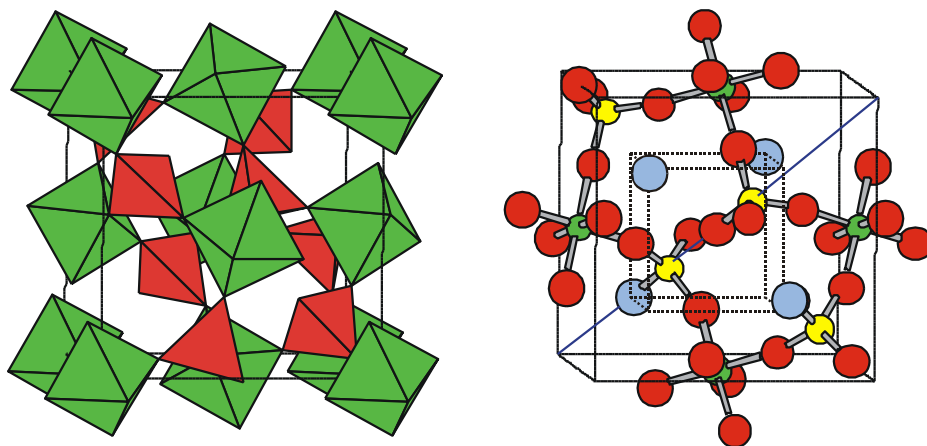
Figure 2.5 The structure of cubic ZrW_2O_8: a) Polyhedral representation with ZrO_6^{4+} shown in green and WO_4^{4-} shown in red b) Ball and stick representation showing zirconia (green), tungsten (yellow) and oxygen (red). The mono-coordinated O4 is highlighted in blue.[13]

In the asymmetric unit there are four in equivalent oxygen sites (O1 – O4), two tungsten sites (W1 and W2), and one zirconium site (Zr1). Each $W_2O_8^{4-}$ groups lie along three-fold axis of the body diagonal of the unit cell and consists of two crystallographically distinct WO_2^{2-} tetrahedral. In each WO_4^{2-} units, three oxygens (O1 and O2 for tetrahedra containing W1 and W2 respectively) are two coordinate and are shared with ZrO_6 octahedra. The remaining oxygens (O4 and O3) are formally one coordinate and this leads to the flexibility of the framework. However, there is a weak interaction between O3 and W1 with a bond length of ~ 2.4 Å while O4 has a distance to W2 of ~3.6 Å. The two WO_4^{2-} groups point along the body diagonal in the same direction.

Mary *et al.*[11] discovered that the material undergoes NTE from 0.3 K up to 1050 K, its decomposition temperature, as shown in (Figure 2.6). The NTE is strongly negative, with α_1 having a value of -9.07 x 10^{-6} K^{-1} (0-350 K)[14]. The material undergoes a phase transition at ~ 430 K. The cubic nature of the structure means NTE occurs isotropically over the entire range.
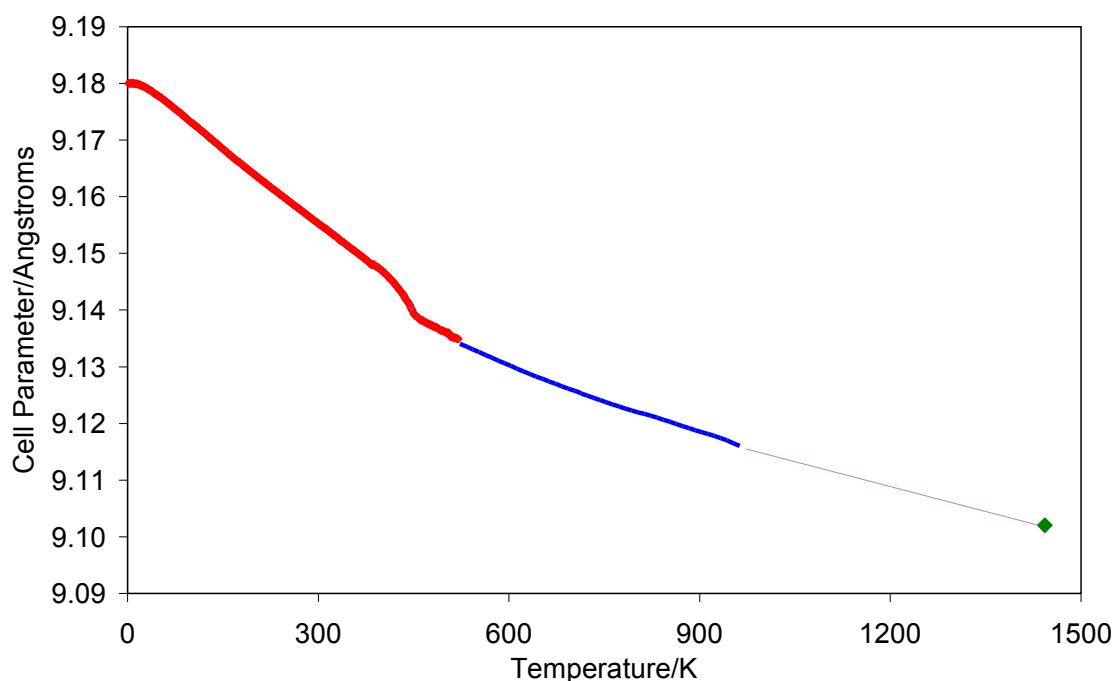
Figure 2.6 The cubic *c* cell parameter of ZrW_2O_8 as a function of temperature to illustrate the thermal behaviour obtained by neutron diffraction (red), dilatometry (blue) and high temperature neutron diffraction (green). The dashed line is the temperature range in which ZrW_2O_8 is thermodynamically unstable.[13]

This phenomenon has attracted a lot of interest due to the wide temperature range, either side of room temperature, in which ZrW_2O_8 exhibits NTE. As a result ZrW_2O_8 could be potentially used in composite materials, which may be tailored to have a certain NTE coefficient.

The slight change in the cell parameter at ~450 K (Figure 2.6) is due to an order-disorder phase transition. The high temperature phase, β-ZrW_2O_8, is essentially the same at the α-form, however, the WO_4^{2-} units have disordered directions and the introduction of an inversion centre means the β-phase has higher symmetry and

Pa3 space group. The two different orientations of $W_2O_8^{4-}$ are illustrated in Figure 2.7.
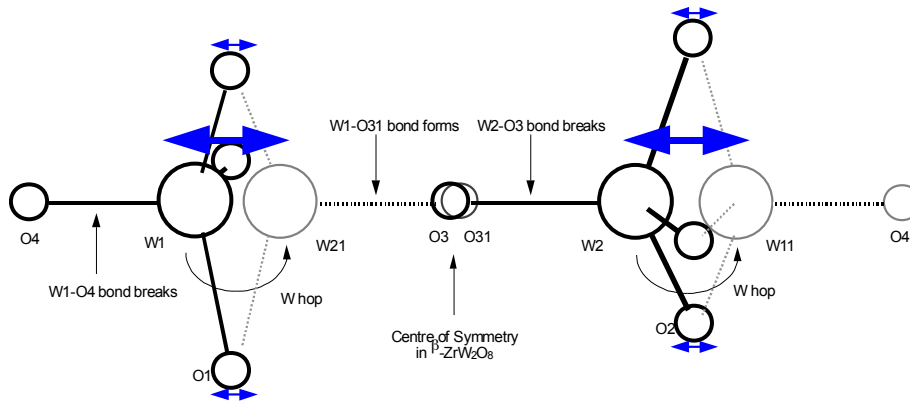
Figure 2.7 A schematic diagram of the two possible WO_4^{2-} orientations in the ordered-disordered phase. The α-phase is ordered and the WO_4^{2-} lie along the same direction (bold bonds) while the β-phase is disordered (bold and dashed bonds).[3]

A structural model in *P2₁3* which allows both WO_4^{2-} orientations was used for the fitting of the variable temperature neutron powder diffraction data by Rietveld refinement. The presence of two different orientation results in a fractional occupancy parameter for each orientation. In the fully ordered α-phase the fractional occupancy is equal to 0 or 1, while the fully disordered β-phase has a fractional occupancy of 0.5. The variation in fractional occupancy parameter as a function of temperature (Figure 2.8) can be used to monitor the phase transitions. The smooth decrease in ordering suggests oxygen mobility (*i.e.* net movement of O4) occurring at lower temperatures than in most oxygen ion conductors.
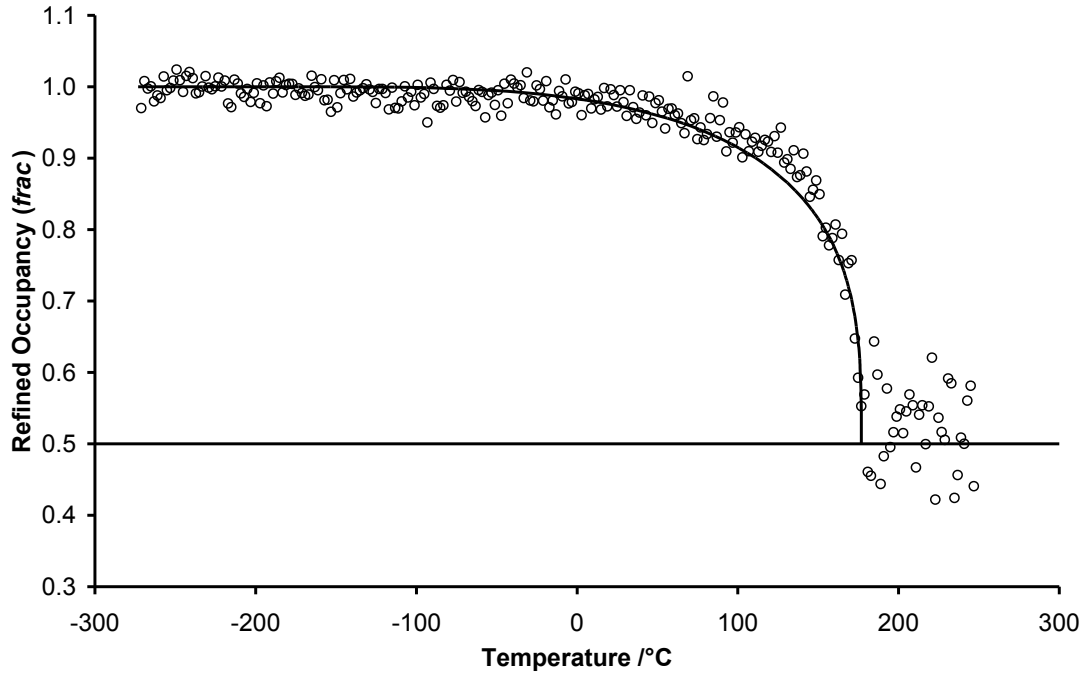
Figure 2.8 The O(4) fractional occupancy parameter as a function of temperature from neutron diffraction data of ZrW_2O_8.3

Hampson *et al.*[15,16] investigated the oxygen mobility. They proposed that the S_N2 type mechanism for oxygen mobility illustrated in Figure 1.9 was incorrect and the 'ratcheting' model which involved the 'flipping' of WO_4^{4-} tetrahedral along the diagonal of the cube was more likely to be the correct model. Soleilhavoup *et al.*[17] used *ab initio* calculations to quantify the oxygen mobility with experimental data (Section 1.6).
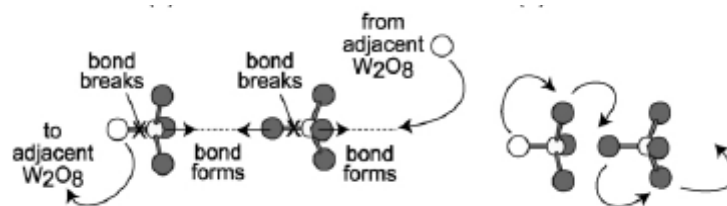
Figure 2.9 The S_N2-like model (left) and the 'ratcheting' mechanism (right) which was shown to be responsible for the oxygen mobility for the α to β phase in ZrW_2O_8[15]

The flexible Zr-O-W link accounts for the NTE as confirmed by Evans *et al*[14]. They proved that NTE is related to transverse vibrations of the bridging oxygen atoms in this link. The presence of RUMs (Section 1.3) leads to coupled rotations of the

13

relatively stiff polyhedra which leads to the overall decrease in volume. RUM calculations performed by Pryde *et al*[18-20]. quantified this and proved that low energy transverse vibrations are present and confirmed the minor change at the α-β phase transition. Cao *et al.*[21,22] have, however, argued that the RUM model in α-ZrW_2O_8 is incorrect. They performed X-ray absorption fine structure (XAFS) measurements to investigate the local environment around Zr and W atoms. They suggested that heavy atom motion also contributes to the low energy vibrational mode and NTE was cause by the correlated movement between the WO_4^{4-} tetrahedral and ZrO_6 octahedral while the Zr-O-W linkages remained relatively rigid. Tucker *et al.*[23] used reverse Monte Carlo modelling which resulted in favouring the RUM model rather than Cao *et al.*'s model.

Mary and Evans[11] have reported that cubic HfW_2O_8 behaves in a similar manner to cubic ZrW_2O_8 and they are iso-structural due to the similarity of the powder patterns. The isotropic NTE occurs over a large temperature range and the α/β phase transition occurs at the same temperature. This proves that NTE is not affected by the species of the cation but the existence of flexible A-O-M linkages.

$ZrMo_2O_8$

Cubic $ZrMo_2O_8$ was first reported by Lind *et al.*[24] in 1998 and synthesised from the dehydration of the precursor $ZrMo_2O_7(OH)_2.2H_2O$. The room temperature cubic phase, γ-$ZrMo_2O_8$, is isostructural with β-ZrW_2O_8, however, it is not thermodynamically stable and hence it is difficult to synthesis phase pure cubic material. The dominant phase is the trigonal polymorph which occurs above ~ 873 K as shown by the phase diagram for $ZrMo_2O_8$ (Figure 2.10)
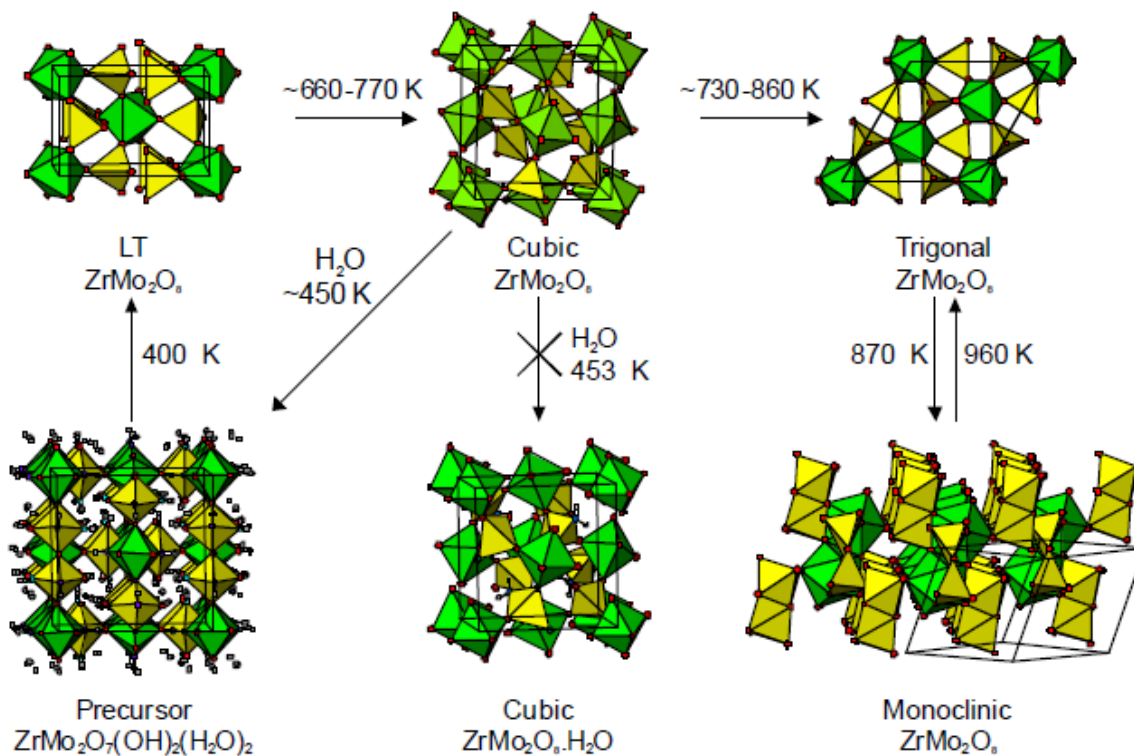
Figure 2.10 Ambient pressure phases of ZrMo$_2$O$_8$.[13]

Lind *et al.*[24] investigated the thermal expansion using variable temperature X-ray and neutron diffraction (Figure 2.11) and showed that it exhibits isotropic NTE with an average expansion coefficient of -6.9 x 10^{-6} K^{-1} between 2 and 300 K and -5.0 x 10^{-6} K^{-1} between 250 and 502 K. The absence of any discontinuities in the cell parameter as a function of temperature illustrates that no order-disorder phase transitions were present.
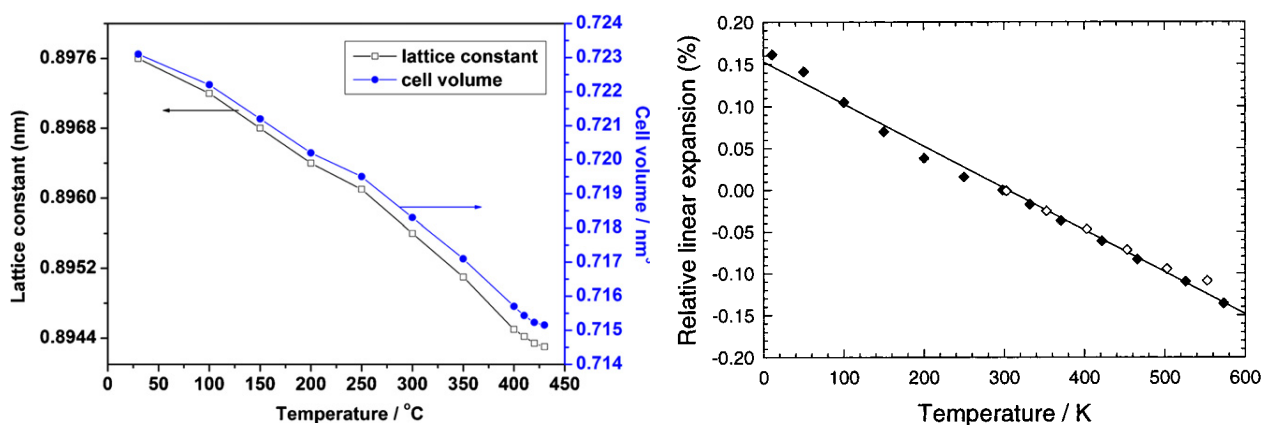
Figure 2.11 Thermal expansion of cubic ZrMo$_2$O$_8$ obtained by Lind *et al.*[24]

Evans, Allen *et al.*[25] investigated this further and characterised the metastable intermediate polymorph of $ZrMo_2O_8$ as known as LT-phase (Low-Temperature phase). They used XRD and neutron diffraction data to determine the structure. They showed that there are 6 in-equivalent O atoms in the asymmetric unit. From variable temperature XRD they showed that the LT phase is a NTE material which displays bulk contraction with α_1 = - 1.2 x 10^{-6} K^{-1} between 100 and 500 K. Figure 2.12 shows that the cubic phase can be synthesised over the thermodynamic trigonal phase. This shows that the LT phase can be an intermediate phase through to the cubic phase. Allen *et al.*[3] show that by characterising the structure of LT phase it provides insight to why the kinetically favoured cubic phase is favoured over the trigonal phase and the kinetics of the transformation from LT to cubic are thought to be faster than those for the drastic atomic rearrangements that are required to form the trigonal phase.
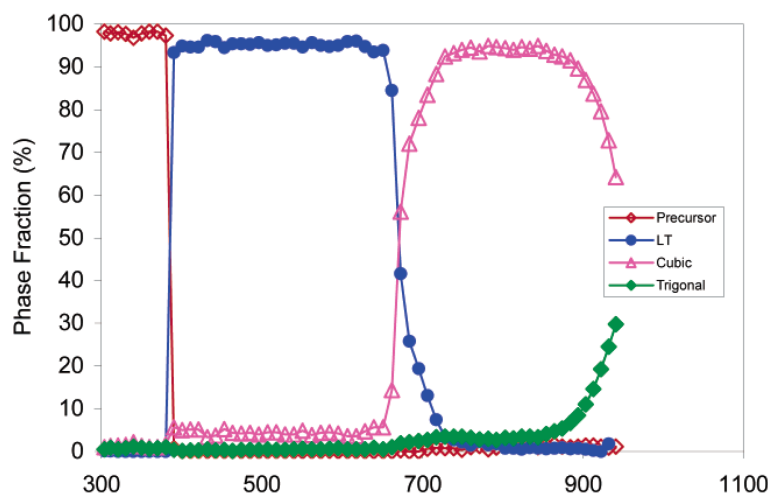
Figure 2.12 Percentage composition as a function of temperature for variable temperature powder X-ray diffraction experiments on perchloric acid derived $ZrMo_2O_7(OH)_2.2H_2O$ obtained by Allen.[3]

Allen and Evans[26;27] used high precision neutron diffraction to show that at temperatures above 200 K, the cell parameters upon warming and cooling $ZrMo_2O_8$ are in close agreement (approx. < 0.0002 Å) as shown by the overlap in the cell parameters (Figure 2.13). Although at temperatures lower than 200 K there are slight discrepancies between slow-cooled and quench-warmed cell parameters through loss of low levels of water or partial sample reduction. There is an

irreversible sample change between 502 and 200 K that does not account for the cell parameter discrepancies. This is shown by the differences in the thermal expansion (Figure 2.14) when the sample of cubic $ZrMo_2O_8$ is slow-cooled and quenched-warmed. When the sample is slow-cooled there is a much gradual change in the thermal expansion, whereas the quenched-warmed thermal expansion occurs at a much greater rate with α changing from ~ -8 x 10 $^{-6}$ K^{-1} at 200 K to -5.5 x 10^{-6} K^{-1} at 240 K.
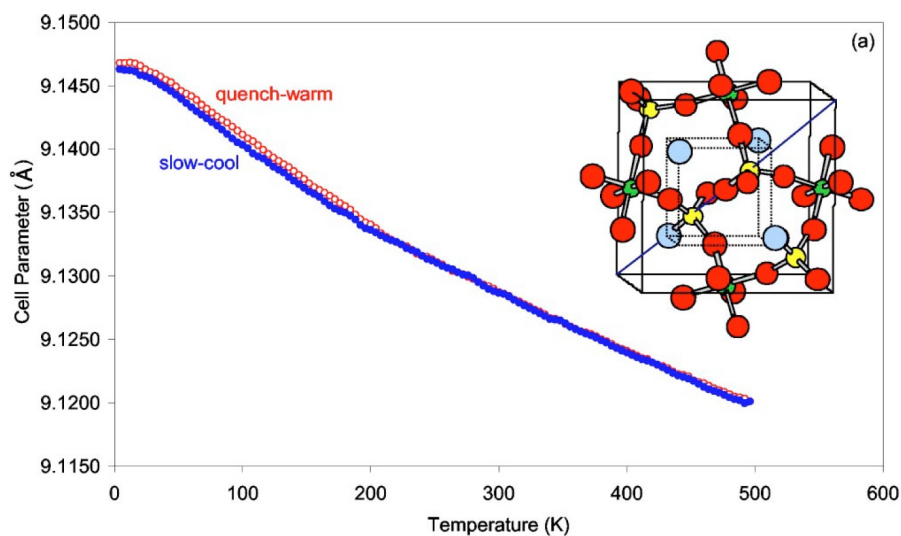
Figure 2.13 The *a* lattice cell parameter for $ZrMo_2O_8$ upon warming (red) and cooling (blue) obtained by Evans *et al.* using variable temperature neutron diffraction experiments.[26]
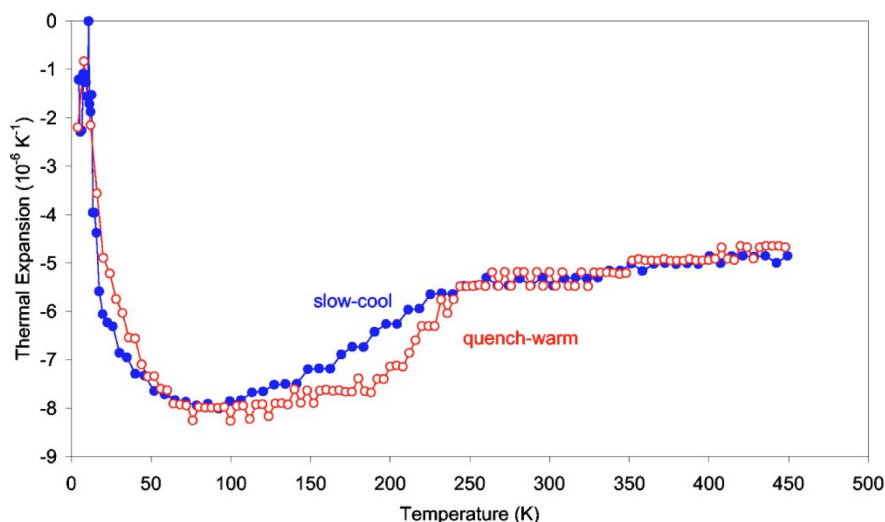
Figure 2.14 Changes in thermal expansion when cubic ZrMo₂O₈ is slow-cooled and quench-warmed.[26]

Allen[3] also showed comparisons of the thermal expansion between $ZrMo_2O_8$, ZrW_2O_8 and $ZrWMoO_8$. A change in thermal expansion from less than - 9 x 10^{-6} K^{-1} in the oxygen ordered form to around – 6 x 10^{-6} K^{-1} in the dynamically disordered β form occurs for ZrW_2O_8. Similar changes occur for α-$ZrWMoO_8$. The expansion co-efficient of the statically disordered β/partially ordered α-$ZrWMoO_8$ changes from ~ - 9 x 10^{-6} K^{-1} to – 5.5 x 10^{-6} K^{-1} when dynamic oxygen disordering occurs. In both these compounds the onset of oxygen disorder occurs at the phase transition. The thermal expansion co-efficient for γ-$ZrMo_2O_8$ thus gives a strong indication to a change from static to dynamic oxygen disorder at ~ 200 K. Full Rietveld refinement showed that there were no changes in the atomic coordinates / occupancies / temperature factors at this temp. This confirms the indication that the phase transition is between a static and dynamic disordered oxygen configuration.

Lind *et al.*[24] varied the acid used to synthesise the precursor, $ZrMo_2O_7(OH)_2.2H_2O$. Changing the acids used (hydrochloric acid, perchloric acid and nitric acid), changes the particle size and morphology as shown by the SEM images (Figure 2.15) and is also discussed in Section 4.2. Lind *et al.*[28] also demonstrated that the cubic phase can only be formed via the low temperature (LT) phase as shown by the phase diagram in Figure 2.15.
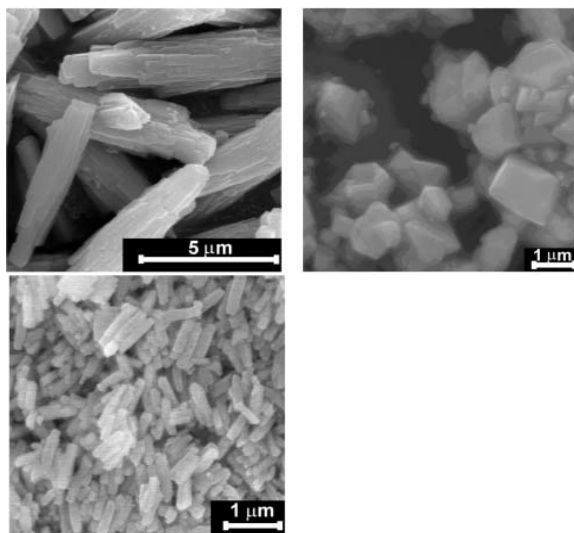
Figure 2.15 Cubic ZrMo₂O₈ prepared by Lind *et al*. in a chloride environment (top left), in a nitrate environment (top right) and in a perchlorate environment (bottom left).[28]

Readman *et al.*[29] were able to synthesise the cubic polymorph directly from constituent oxides by firing the constituent oxides at high temperatures (~1450 K) for a few seconds followed by rapid quenching. The cubic polymorph had previously been assumed to be thermodynamically meta-stable at all temperatures. Recently Liu *et al.*[30] were able to synthesis cubic $ZrMo_2O_8$ using a sol-gel method in high purity. They showed from XRD data the cubic β-$ZrMo_2O_8$ film adopts the β-$ZrMo_2O_8$ structure. The lattice parameters (a = 8.976 Å) obtained were smaller than pure cubic β-$ZrMo_2O_8$ powders (9.1304 Å[24] and 9.1472 Å[27]). The differences in the preparation could have led to the differences in the lattice parameters. The SEM images obtained for the gel films shows the absence of any significant grain growth which differs to those obtained by Lind *et al.* AFM suggests that the particle size of the sol-gel is approximately 100 nm. The film was shown to exhibit NTE between 293 and 703 K (Figure 9) and the average linear thermal expansion coefficient of cubic β-$ZrMo_2O_8$ film was calculated to be -8.66 x 10^{-6} K^{-1}.

2.5 ^{17}O NMR Spectroscopy

Oxygen is of particular importance to materials technology as it is prevalent in inorganic compounds. It is considered the most chemically and biologically important elements as it can form compounds with almost all elements apart from a few noble gases and metals. The structure and dynamics of oxygen-containing

compounds is of great significance and thus makes oxygen nucleus very interesting to investigate. However, compared to other nuclei such as ^{1}H, ^{13}C, ^{15}N, ^{31}P and ^{19}F, ^{17}O has received relatively little attention as compounds need to be enriched with NMR-sensitive ^{17}O NMR.

Oxygen has three stable isotopes: ^{16}O, ^{17}O and ^{18}O with 99.76 %, 0.037 % and 0.2 % abundance respectively. Of the three stable isotopes only ^{17}O possesses a non-zero spin (I = 5/2) and therefore is the only isotope accessible to NMR. Another challenge is the low natural abundance of ^{17}O isotope and the low absolute sensitivity compared to that of ^{1}H (~1.1 x 10^{-5}) which makes it more difficult to investigate; isotopic enrichment is needed. The high cost of ^{17}O enriched water or gas needed to acquire high resolution spectra has hindered studies using ^{17}O nucleus. ^{17}O is also a quadrupolar nucleus (detailed in Chapter 2) and broadening of the NMR signal due to second-order quadrupolar effects can complicate the interpretation of the data. The principles and applications of ^{17}O NMR have been previously reviewed.[31]

Structural information can be determined from quadrupolar and chemical shift parameters. In order for the extraction of structural information (qualitative or quantitative) high-resolution NMR spectra are a pre-requisite. Removal of anisotropic broadening allows the distinct number of crystallographic sites to be determined and thus provides information into which space groups are possible and hence the number of structures. Quadrupolar and chemical shift interactions, C_Q, η_Q and δ_{iso}, can also be extracted from high resolution NMR spectra and in some cases the chemical shift anisotropy (CSA). These interactions are dependent on the local environment and hence provide information about the structure.

Obtaining spectra at different magnetic fields can provide insights into structural features that are not possible at lower magnetic fields. It is now possible to obtain spectra at magnetic fields as high as 21.1 T [32,33]. One such example to show the increase in structural features seen as magnetic field increases is the NMR spectra for $CaAl_2O_4$ (Figure 2.16)[33]. At the smaller 9.4 T magnetic field no distinct peaks or

shoulders are present. Increasing the magnetic field to 21.1 T, 9 distinct peaks and shoulders are seen from 12 crystallographic sites.
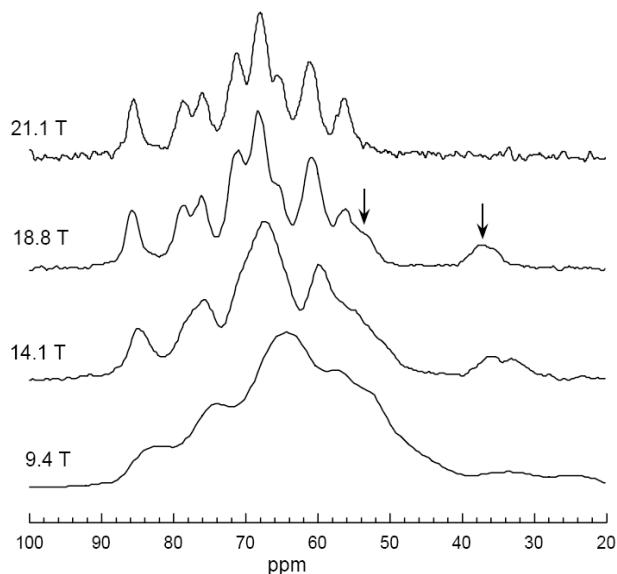
Figure 2.16 ^{17}**O MAS NMR spectra for CaAl$_2$O$_4$, The arrows indicate the major peaks of CaAl$_4$O$_7$ (impurity).**[33]

In some cases, the spectrum from higher magnetic fields seem to show no second order quadrupolar features, although, upon analysis of spectra at lower magnetic fields is shown that this may be misleading. CaTiSO$_5$ has 4 distinct O environments and the ^{17}O MAS NMR (Figure 2.17) shows Ti-O-Ti region of the spectra. At the high 21.1 T magnetic field nsecond order quadrupolar lineshapes are not seen but the 18.8 T spectrum shows that the second order quadrupolar shifts of the central transision peaks are still as large as 4-5 ppm in 21.1 T spectrum[33].
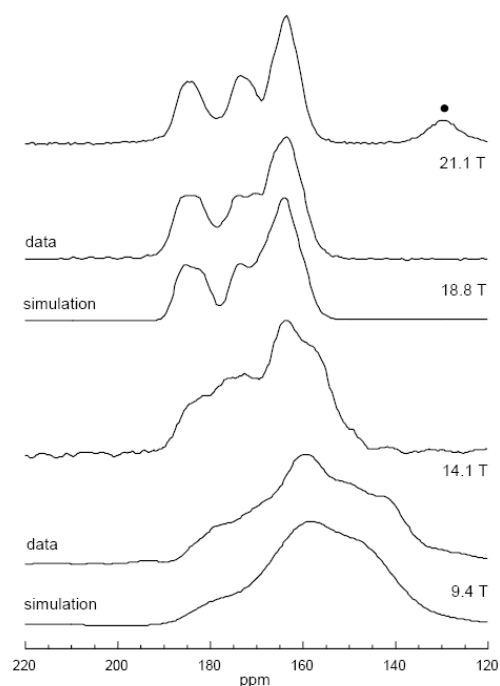
Figure 2.17 ^{17}O MAS NMR spectra for the central transitions for Si-O-Ti sites in CaTiSiO$_5$ and the simulations of spectra at 18.8 T and 9.4 T.[33]

It has been shown that the isotropic chemical shift is dependent on structural parameters such as the bond distance and bond angles. In ionic pervoskites, ABO$_3$ and A$_2$BO$_3$, where A = Li, Na, Ca, Sr, Ba and La and B = Ti, Zr, Sn, Nb, Al, the changes in the chemical shift were influenced by the nature of the B ion and hence the polarising power and M-O bond lengths. It was shown that longer M-O bond lengths gave more positive chemical shift ranges[34]. For example the chemical range of zirconates, 298-376 ppm was lower than in titanates, 372-564 ppm for average bond lengths of 2.093 Å and 1.995 Å respectively. The strong dependence between bond distance and δ_{iso} has been exhibited in a range of silicate materials[35].

Quadrupolar coupling (C_Q) also has a dependence on the structural parameters. Schraumm *et al.*[36] showed that as the iconicity of M-O bond decreases C_Q increases. In silicates this dependence has been used to study between bridging (Si-O-Si) and non-bridging (Si-O-Mg) oxygen. The different types of oxygens have different C_Q values, 4-6 MHz and 2 MHz respectively and these can be identified. In the case of MgSiO$_3$, the structure has been identified as a chain silicate due to the C_Q values extracted from MQMAS ^{17}O NMR spectrum. 4 of the O environments

have C_Q values between 4-5 MHz corresponding to bridging oxygen and the other 2 O environments correspond to non-bridging oxygen with C_Q values of ~ 3 MHz.[35]

2.6 *Ab Initio* Calculations

Ab inito calculations have been used to assist in establishing trends in ^{17}O quadrupolar and chemical shift parameters on structure. Often the use of *ab initio* calculations is needed due to the difficulty in extraction of these parameters experimentally.

Calculations of these NMR parameters involve some approximations of the electrons and nuclei and the way that they respond to the presence of a magnetic field. One such approximation is the Hartree Fock (HF) approximation where the electron is assumed to be moving independently in the mean of the field generated by other electrons and the electron-electron repulsions are treated in an 'average' way. Another is the density functional theory (DFT) method in which the problem of electron correlation is reduced to finding an appropriate (and approximate) form for the functional used to describe exchange.. Although approximations are required to calculate the NMR parameters, excellent results can be achieved and used to compare to experimental results or when experimental results are not available.

Tossel *et al.*[37-39] used simple cluster models to calculate the NMR parameters and study ^{17}O trends using HF approximations. ^{17}O NMR calculations have been used to study silicate glasses and its analogues. Simple cluster calculations showed that there was a strong correlation between C_Q and electro-negativity of the co-ordinated cations in crystalline silicates. The use of NMR calculations and further refinements in *ab initio* calculations have enabled other trends in ^{17}O quadrupolar coupling parameters and structural features to become apparent[17,40,41]. Using GAUSSIAN 94 it was shown that in silicates, the Si-O bridging distance affects the C_Q and the angle of Si-O-Si affects the asymmetry parameter in $(OH)_3Si$-O-$Si(OH)_3$ cluster.[42]

In M-O-M units the effect of the first co-ordinating cation largely influences the C_Q and the second co-ordinating cation much less so[40-42]. Xue and Kanzaki[43] confirmed this by extending the cluster to 4 co-ordinate spheres and there was very little

23

difference in the C_Q values when 4 coordination spheres is taken into account compared to 1 coordination sphere. However, large coordination spheres are needed to calculate accurate chemical shifts and so the calculation of C_Q is a much more economical way to provide structural information.

A better approach to calculate quadrupolar coupling parameters and chemical shifts is the use of DFT methods. Pickard *et al.*[44] calculated the [17]O quadrupole and chemical shift parameters in a series of SiO_2 polymorphs.

Charpentier *et al*[45] showed that the trends in the calculation of ^{17}O, ^{29}Si and ^{23}Na NMR parameters in a series of sodium silicate crystalline materials could be applied to study silicate glasses (for which a lot less structural information is known).

Soleilhavoup *et al.*[17] used the CASTEP[46] programme to calculate the ^{17}O NMR parameters for α-ZrW_2O_8. They used *ab initio* calculations to make correlations between [17]O chemical shifts and local structure. The calculated spectrum was simulated from the calculated parameters and the calculated and experimental shifts were compared. It was shown that there is no significant effect on the spacing of δ_{iso} values when changes in the unit cell parameters occurred. However, [17]O chemical shifts were extremely sensitive to changes in individual internal coordinates and hence could be used to characterise subtle structural distortions in oxide materials. It was also shown that these [17]O chemical shifts were strongly dependent on the local oxygen atom environment. Furthermore, there is a direct correlation between the chemical shift and either W-O bond length or the local bond asymmetry. In both cases as the W-O bond length or local bond asymmetry increases, the frequency of the chemical shift increases. This is also true for the structural parameters and the quadrupolar coupling.

2.7 Oxygen mobility

There has been much investigation into the oxygen dynamics in ionic conductors. There are a growing number of applications of ionic conductors, for instance in catalytic convertors, membranes for oxygen/nitrogen separation and as electrolytes in solid oxide fuel cells (SOFCs). All these applications need a high level of O^{2-}

mobility and currently the useful conductivity of the materials is limited to high temperature (greater than 800 $^{\circ}$C). Investigation into finding conducting materials at lower temperature is important as is characterisation and understanding of the structural factors which control the conductivity.

^{17}O NMR probes into the local oxygen environment and provides localised information about the oxygen sites. NMR can be used to investigate dynamic processes although prior to 2002 it had not been commonly used to investigate oxide ion motion due to the low oxide ion conduction of most oxides. Most magic angle spinning (MAS) NMR probes can only reach 250 $^{\circ}$C while static probes can reach higher temperature but spectral resolution is lost. Oxide ion dynamics have been investigated with other methods such as AC spectroscopy and impedance studies, although these methods measure the bulk properties and not the localised information that can be obtained from NMR studies. Different dynamic models can be distinguished using various NMR experiments such as 2D EXSY, as discussed in this section. Diffraction methods cannot be readily used to distinguish different motional models as the overall electron density is independent of motional mechanism. Obtaining qualitative results using ^{17}O solid state NMR is relatively straight-forward where the dynamics involve sites with resolved NMR frequency. Quantitative results, such as exchange rate as a function of temperature, are more challenging due to the quadrupolar nature of ^{17}O.

Chapter 3 Characterisation techniques

3.1 X-Ray Diffraction (XRD)

X-Ray diffraction is a very powerful structural characterisation method that can be used to determine the full structure of a material. Diffraction occurs when a wave interacts with a solid object or passes through a gap between two objects. If the wavelength is the same order of magnitude as the object or gap, the interaction may give rise to interference. X-rays have a wavelength of approximately 1 Å. This is approximately the same size as an atom. The basis of X-ray diffraction is then that the X-rays have a similar wavelength to the inter-atomic spacing of the crystal structure. The X-rays interact with the electrons in the atoms in the crystal structure and can be scattered in all directions. In most directions the X-rays have zero intensity due to destructive interference. However, in some directions constructive interference occurs and the resultant intensity of the X-rays is reinforced and these can be recorded as a diffraction pattern.

A crystal structure can be described in terms of a lattice. This is an array of identical points which are equivalent by translational symmetry. A motif is a small group of atoms, a molecule or a collection of several molecules which can be associated to each of the lattice points and which lead to the overall arrangement of the crystal structure. The unit cell of the structure is defined as the smallest repeating unit that represents the entire structure. The unit cell parameters can be defined as three lattice vectors **a**, **b** and **c** with angles α, β and γ. Fractional co-ordinates are used to describe the positions of atoms within the unit cell. Miller indices are used to describe the lattice planes of a crystal and are denoted *hkl*. A family of lattice planes can be described as a group of lattice planes that are parallel to each other with equal spacing. If one plane passes through the origin, the next parallel plane crosses the axis at *a/h*, *b/k* and *c/l*. The diffraction of X-rays can be described in terms of the lattice planes and Braggs Law can be used to describe the constructive interference and predict the direction of the diffracted beams.

$$n\lambda = 2d_{hkl}sin\theta_{hkl}$$
<div align="right">**Equation 3.1**</div>

Where:

n = integer (the order of reflection or diffraction and this is normally incorporated into the lattice plane symbol and thus normally omitted from the equation)

λ = wavelength

d_{hkl} = inter-planar spacing in terms of the lattice plane

θ = incident angle with respect to the planes.

Bragg's law applies to a crystal system irrespective of the positions of the atoms and only the inter-planar spacing is important. Figure 3.1 shows that the X-rays can be considered geometrically as being reflected from a set of parallel. The angles of incident and reflection must be equal. The reflection from adjacent planes gives rise to interference and when the path difference of X-rays reflected from two planes is an integer multiple of *λ*, the Bragg equation is satisfied. When the X-rays are scattered by atoms in the same plane the path difference is zero. The reflection is recorded at *2θ* and the corresponding d_{hkl} can be calculated. Structural information can be deduced from the diffraction patterns. The peak positions give information about the size, shape and symmetry of the cell while the intensity gives information about the electron densities and hence the atomic positions within the cell.

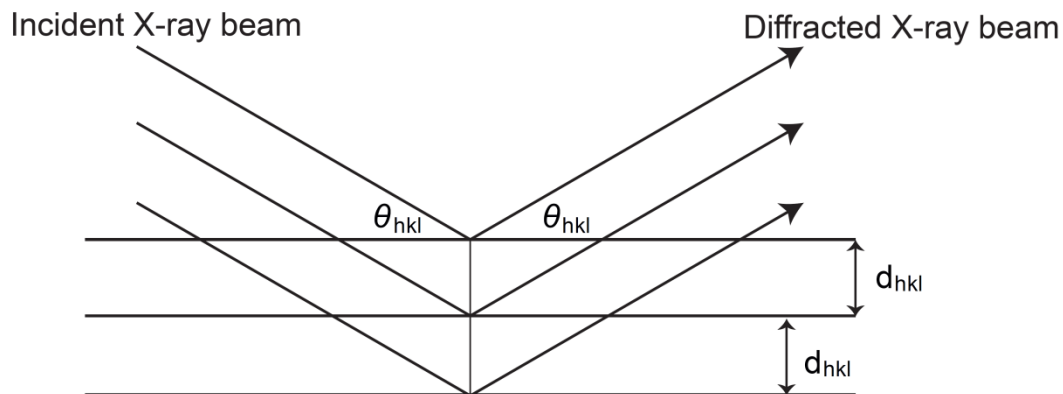**Figure 3.1 The Bragg construction for diffraction by three-dimensional crystal structure; one set of parallel lattice planes is seen edge-on.**

Powder X-Ray Diffraction (PXRD)

The principle behind powder XRD is that a (usually) monochromatic beam of X-rays (fixed *λ*) is focused on to a finely powdered sample. The sample should have

randomly orientated crystals otherwise the problem of preferred orientation arises. If the crystals are randomly orientated, some of them will satisfy Braggs law (Equation 2.1) and diffraction will occur for these crystals and planes. The sample may be prepared either as a bulk powder or as thin layers of fine powders sprinkled onto a silica disc which has been smeared with Vaseline. This ensures that the sample contains a random orientation of crystals and thus reduces the problem of preferred orientation.

The diffracted beams may be detected by several methods:

1. With a strip of photographic film (Debye-Scherrer and Guinier focusing methods)
2. Geiger counter or scintillation counter that is linked to a computer (diffractometer).

In this thesis linear PSDs were used to detect the diffracted beams.

The powder XRD diffractometer scans a range of *2θ* at constant angular velocity. It is common to refer to the angle between the incident and reflected beam as *2θ* and the common range of *2θ* used is 10 – 80 ^{o} *2θ* as this is sufficient to cover the most useful part of the diffraction pattern.

Powder XRD can give good qualitative identification of a crystalline phase or compound. However, no direct information about the chemical composition can be given. It is useful as each crystalline phase gives a characteristic powder pattern that can be used for identification. The two variables used in powder XRD are the peak position and the intensity of the peak. The peak position is quantitative as the d_{hkl} spacings can be measured accurately. High angle diffraction methods give the most accurate d_{hkl} spacing measurements as high *2θ* angle reflections are most sensitive to small variations in the d_{hkl} spacings. The intensity of the peak can be either qualitative or quantitative and be taken as peak heights or peak areas.

Powder XRD loses much of the information that is available in single crystal diffraction as the information is compressed into one dimension. The reliance on randomly orientated crystallites being present in the sample, some of which being in the correct orientation to diffract at the Bragg angle also is a disadvantage.

However, there are advantages of using powder XRD compared to single crystal diffraction. Single crystals can be extremely difficult to obtain and powdered samples are easier and thus a large range of compounds can be studied. During structural transitions, single crystals tend to shatter whereas powder samples are more robust and variable temperature, pressure and chemical environment studies can be performed.

Bruker AXS d8 Advance X-ray powder diffractometers

Two Bruker diffractometers operating at 40 kV and and 40 mA have been used during this project. The 'd8' provides strictly $CuK_{\alpha1}$ radiation using a Ge(111) crystal monochromator. The X-rays pass through a fixed Soller slit and fixed 1 ^{o} divergence slit. The diffracted intensity is detected by a Vantec linear Position Sensitive Detector (PSD) with minimum step size of 0.0085 ^{o}, using XRD Commander. High temperature XRD experiments have been carried out using an Anton Parr HTK 1200 furnace attached to this machine. This attachment allowed for reactions to be studied up to 1500 K.

As with the 'd8', the 'd9' also uses a Cu tube providing $CuK_{\alpha1, 2}$ radiation, Soller slits and incident and diffracting variable divergence and anti-scatter slits. The detector used on this machine is a Vantec linear positions sensitive detector.

Siemens d5000 Powder Diffractometer

The Siemens d5000 diffractometer is an automated diffractometer operating at 40 kV and 40 mA. A $CuK_{\alpha1, 2}$ source produces X-rays which pass through a Soller slit first and then either a fixed one degree or a variable divergence slit (giving a 6 mm or 20 mm illuminating lengths). The diffracted X-ray beams pass through a second Soller slit and then are reflected by a graphite monochromator and enter a the scintillation counter.

3.2 Rietveld Refinement[47,48]

The Rietveld method is a method to refine crystal structures by extracting detailed crystal structure information from X-ray powder diffraction data. It is based on least-squares refinement which minimises the difference between the observed and

calculated diffraction patterns, not the individual reflections, until a 'best fit' can be achieved. This method allows a structural model to be fitted to the experimental powder diffraction data.

The diffraction pattern must be digitised and is recorded as intensity, y_{obsi} at each increment i. The increments may be the scattering angle, 2θ, or an energy parameter such as velocity (for time-of-flight neutron data). In this thesis a constant wavelength of X-rays was used to collect the powder diffraction data and hence y_{obsi} was collected at each experimental value of 2θ. Typical step sizes are in the range 0.01 to 0.05 2θ for fixed wavelength powder diffraction data.

As mentioned above, this method uses a least-squares fit to all the intensities, y_i, simultaneously. The residual, S_y, is the quantity that is minimised by this method as given in Equation 2.1.

$$S_y = \sum_i w_i (y_i - y_{ci})^2$$

Equation 3.2

Where:

$w_i = 1/y_i$

y_i = observed intensity at ith step

y_{ci} = calculated intensity at ith step

This method is a structure refinement method and not a structure solution method. It is important to start with a reasonably good starting model as the observed intensities are not allocated to particular Bragg reflections, nor are overlapped reflections resolved beforehand. Many Bragg reflections contribute to the calculated intensity, y_i, at each point. The calculated intensities are determined by Equation 2.2:

$$y_{ci} = S \sum_K L_K |F_K|^2 \phi (2\theta_i - 2\theta_k) P_K A + y_{bi}$$

Equation 3.3

Where:

S = scale factor

30

K = Miller indices *h, k, l* for the Bragg reflection

L_K = contains the Lorentz, polarisation and multiplicity factors

Φ = reflection profile function

P_K = preferred orientation function

A = absorption factor

F_K = structure factor for the Kth Bragg reflection

y_{bi} = background intensity at the *i*th step.

The calculated shifts are applied to the initial parameters to produce an improved model and this is repeated until a global minimum is reached. It is important that the starting model is close to the correct model otherwise the global minimum may not be reached and a local or false minimum found. Multiple phases may be refined simultaneously and analysis of the separate scale factors can provide quantitative phase analysis. Table 3.1 shows the parameters that are refined simultaneously. These can be divided into 2 groups, depending on whether they are phase specific or global.

Global Parameters	Phase Specific
Sample Height	Scale Factor
Background	Lattice Parameters
Instrumental Parameters	Atomic Coordinates
Profile Asymmetry	Isotropic or Anisotropic Displacement parameters
Absorption	Preferred Orientation
	Peak shape
	Crystallite Size and Microstrain

Table 3.1 Parameters refined during Rietveld analysis.

Preferred orientation occurs when the crystallites in a sample orientate in a particular direction, reducing the randomness of the orientation. This is a problem than can arise from PXRD and false intensity information is obtained. Preferred orientation occurs when the sample is packed into a flat specimen holder backed by a glass slide. To correct this problem, mathematically corrections can be applied so that the

distortions are modelled with 'preferred orientation functions'. Spherical harmonics, as used in this thesis, can also be used and expand the orientation distribution in spherical harmonics. These spherical harmonic functions act as a scaling factor dependent on the *hkl* direction they are modelling.

As with any 'best-fit' method, a criteria is needed to judge and give an indication whether a refinement is proceeding satisfactorily and whether it is sufficiently close to completion and reaching the global minimum. The quality of fit between the calculated and experimentally determined powder diffraction patterns is usually quantified by the residual index (or R-factor). Several R-factors are commonly used such as R-Bragg, R-structure factor, R-profile and R-weighted profile and these are defined below.

The profile residual index, R$_p$ is defined by:

$$\boldsymbol{R_p} = \frac{\sum |y_i - y_{ci}|}{\sum y_i}$$

Equation 3.4

Where:

y_i = intensity of the *i*th data point in the observed pattern

y_{ci} = intensity of the *i*th data point in the calculated pattern

R$_{wp}$ is the weighted profile residual index and is a measure of the whole diffraction pattern as defined by Equation 2.5. From a mathematical point of view this is the most meaningful residual index as the numerator is the residual being minimised and is the best indicator in the progress of the refinement.

$$R_{wp} = \left\{ \sqrt{\frac{\sum w_i (y_i(obs) - y_i(calc))^2}{\sum w_i (y_i(obs))^2}} \right\}$$

Equation 3.5

Where:

w_i = weighting factor for the *i*th data point

R-Bragg and R-structure factor (R$_F$) are biased in favour of the model being used as they are not based on actual Bragg reflections but on intensities deduced from the structural model being used. These residual indices values are, however, useful as

they are the most comparable to the conventional R values quoted for single crystal structural data. Also, as they are based, on the model they are less sensitive to minor misfits in peak shape.

$$R_{Bragg} = \frac{\sum |I_K('obs')-I_K(calc)|}{\sum (I_k(obs))^{\,2}}$$

$$R_F = \frac{\sum |I_K('obs')^{\frac{1}{2}} - I_K(calc)^{\frac{1}{2}}|}{\sum (I_k('obs'))^{\frac{1}{2}}}$$

Where:

I_K = intensity of Bragg reflections with Miller indicies *hkl*.

The goodness of fit, S may be used to judge the quality of fit (Equation2.8). An S value of approximately 3 suggests that the refinement is satisfactory. However, a small value of S does not mean a good fit and the counting statistical errors may be larger than the model errors. This can be accounted for by poor counting statistics or because of high background intensity, which varies smoothly with angle and thus can be easily modelled.

$$S = \left[\frac{S_y}{N-P}\right]^{\frac{1}{2}} = \frac{R_{wp}}{R_{exp}}$$

Where:

R_{exp} = R- expected

$$R_e = \left[\frac{n-P}{\sum w_i y_{oi}^2}\right]^2$$

The use of numerical criteria is important to judge the quality of the refinement. However, it is very important to use these criteria alongside graphical criteria such as difference plots and the calculated and observed diffraction plots. It is often easier to spot immediate errors within in the refinement graphically rather than numerically. A weighted difference plot is also useful as it accentuates the angular trends and gives equal importance to the misfits of both high and low intensity regions as it is defined by:

$$\Delta y_i(weighted) = \frac{\left[\frac{y_i - y_{ci}}{y_i}\right]}{\sigma_i}$$

Equation 3.10

Estimated standard deviation (e.s.d) gives the precision in the Rietveld refinement. The e.s.d is defined as the minimum possible probable error arising from random errors alone and is not the experimental probable error. Sources of systematic errors that do occur are listed in Table 2.2.

Sources of systematic errors
Preferred Orientation
Background
Anisotropic reflection-profile broadening
Profile shapes
Absorption (differs with geometry)
Specimen displacement
Specimen transparency
Extinction
2θ –Zero error
Graininess
Incident beam instability
Instrument electrical or mechanical instability

Table 3.2 List of the sources of systematic errors which occur during the Rietveld refinement.

3.3 Solid State Nuclear Magnetic Resonance (SSNMR)

NMR spectroscopy is an excellent method for investigating the local structure of materials. It uses the interaction between the nuclear spin and a local magnetic field, which is strongly dependent on the local electronic environment of the nucleus. Three factors which contribute to this method being an excellent characterisation technique are:

1. NMR spectroscopy can be applied to a vast majority of samples.

2. Nearly all elements have a spin-active nuclide and the spectra are generally isotope specific as resonances of different nuclei rarely overlap.

3. The resolution can be high under suitable experimental conditions. Small differences in the electronic environment of atoms results in observably different resonance frequencies.

Spin-active nuclides occur when the number of protons and neutrons comprising the nuclei are not paired, resulting in a non-zero spin quantum number, *I,* which can take either integer or half integer values. This spin of the charged nucleus generates a magnetic dipole along the spin axis, the nuclear magnetic moment, *μ*, which is proportional to the spin.

$$\mu = \frac{\gamma I h}{2\pi}$$

Equation 3.11

μ when placed in an external magnetic field, B_0, can only adopt *2I + 1* orientations (or states) with respect to the magnetic field axis which are distinguished by the magnetic quantum number, m_I, where:

m_I = -I, -I + 1,....I – 1, I

In the absence of B_0 the magnetic states are degenerate (*i.e.* have the same energy). When placed in B_0 these magnetic states split:
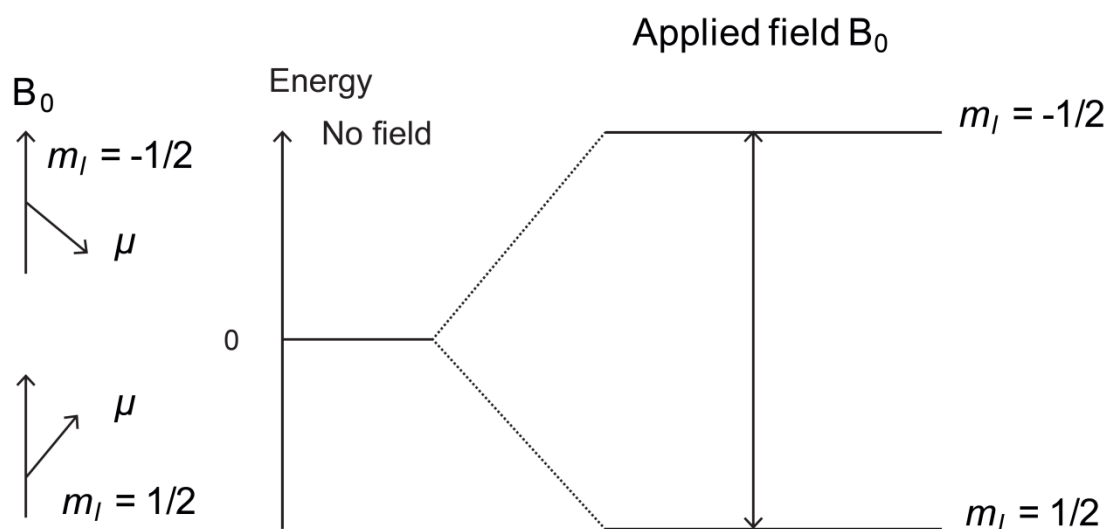
The energy difference between the spin states is given by:

$$\Delta E = \frac{\gamma h B_0}{2\pi}$$

Equation 3.12

and this can be related to NMR frequency (Lamour frequency) by:

$$v_{NMR} = \frac{\gamma B_0}{2\pi}$$

Equation 3.13

These energy differences are very small in comparison to thermal energies, kT, and so the equilibrium (Boltzmann) population differences between the states are extremely small, which largely explains NMR's relatively low sensitivity.

The NMR of the solid state is more complex than solution state NMR. Generally, solution-state NMR spectra, providing the samples are homogeneous and diamagnetic, yield sharp resonance signals compared to the broad complex spectra typically observed in solid samples. The sharp signals arise as the molecules in the solution state are rapidly tumbling randomly at rates fast enough to average out the anisotropic chemical shifts and couplings (Section 2.5). In solid state NMR, all the anisotropic features are retained and the full effects of the anisotropic (orientation-dependent) interactions are observed, resulting in broad complex spectra. However, a potential advantage of solid-state NMR is information on the chemistry, structure and dynamics contained in the anisotropic information which is lost in solution-state NMR. High resolution solid-state NMR spectra can provide the same level and type of information as observed in solution-state NMR, however, special techniques and equipment such as, magic angle spinning (MAS), are needed. These are discussed later in this chapter.

3.4 NMR interactions

Chemical Shift Anisotropy CSA

The chemical shift is the result of the shielding of the nucleus from the applied magnetic field by the surrounding electrons. As a result the chemical shift of a given nucleus depends on its electronic environment. In general, the electrons are not distributed spherically around any given nucleus and so the shielding effect is

36

anisotropic. The shielding, by electrons from the applied magnetic field, in the *z*-axis, σ_{zz}, to the external magnetic field $\boldsymbol{B_0}$ can be described in terms of the anisotropy (ζ) and asymmetry (η):

$$\sigma_{zz}(\theta,\varphi) = \sigma_{iso} + \frac{1}{2}\zeta(3cos^2\theta - 1 - \eta sin^2\theta cos2\varphi)$$ **Equation 3.14**

The Lamour frequency is modified and the chemical shift is dependent on the electronic environment of the nucleus in question. From Equation 2.14 the chemical shift, and thus the resonance frequency, depends on *(3cos²θ-1)* where θ is the angle between the magnetic field and the principal axis about which the chemical shift is defined. Molecular orbitals and crystallographic symmetry dictates the orientation and magnitude of the chemical shielding. At a site of cubic symmetry, the shielding is independent of the sample orientation and a relatively sharp peak is seen. Shielding anisotropies are typically small for ^{1}H but considerable for heavy elements.

In this thesis, powdered samples were used. Powdered samples contain small crystals with a range of orientations with respect to the magnetic field. Hence the chemical shift anisotropy (CSA) will cause dispersions of the peak positions in the NMR spectrum of a powder sample, the spectrum being a sum over individual crystalline orientations. In principle, powder patterns can be fitted to determine the CSA parameters, but this is only possible in practice for simple spectra from high-sensitivity nuclei e.g. ^{31}P (Chapter 6).

Quadrupolar Coupling

Quadrupolar coupling occurs when nuclides have spin quantum number, *I*, greater than ½. These account for over 75 % of all NMR-active nuclei. The study of these nuclei is significantly more difficult than that of nuclei with *I* = ½, although quadrupolar interactions can provide information about the bond lengths, bond angles and site symmetry in the area close to the quadrupolar nucleus.

Nuclei with spin I = ½ have a spherical distribution of positive electric charge. Quadrupolar nuclei differ and have an asymmetric distribution on nucleons giving rise to a non-spherical positive electric charge distribution. Quadrupolar coupling

arises from the interaction of the nuclear electric quadrupole moment with local electric field gradients (EFG) associated with the electronic environment:

nuclear charge distribution

electric field gradients in molecule

Spin-1/2 Nucleus   **Quadrupolar Nucleus**
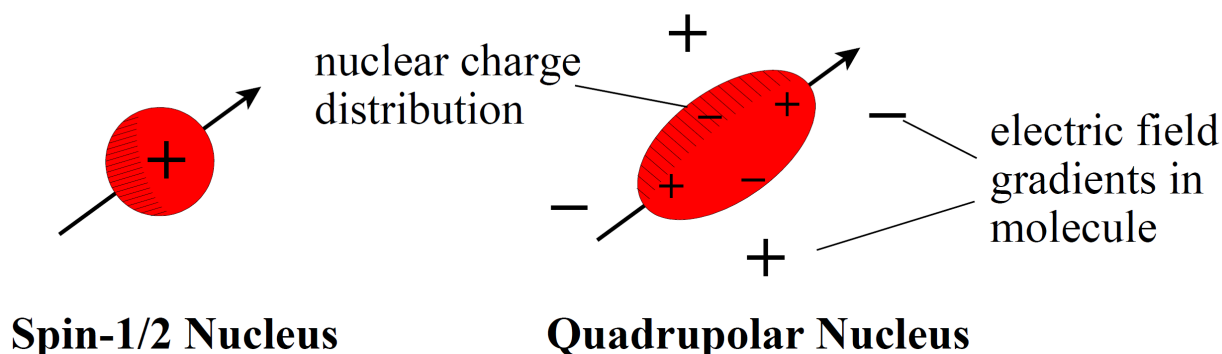
The quadrupolar coupling can have a large range of values depending on the magnitude of the electric quadrupole moment Q and the electric field gradients, q. When the nucleus is at a site of cubic symmetry, the EFG = 0 and the quadrupolar coupling is zero. As the symmetry decreases, the EFG increases and quadrupolar coupling increases. Very large values, hundreds of MHz, are seen in [87]Rb NMR as discussed in Chapter 6. The magnitude of the quadrupolar coupling is given by the by the EFG anisotropy, although it is more common to use the quadrupolar coupling constant, C_Q, which is proportional to EFG anisotropy. The C_Q is characterised by the asymmetry (η).

$$C_Q = \frac{e^2 Q q_{zz}}{h}$$

$$\eta_Q = \frac{q_{yy} - q_{xx}}{q_{zz}}$$

Where q_{xx}, q_{yy} and q_{zz} are the principal components of electric field gradient tensors.

The effect on the quadrupolar coupling interaction on the nuclear spin energies can be described as a perturbation of the Zeeman interaction. In many cases, especially at high fields, B_0, the Zeeman term is dominant. If the quadrupolar interaction becomes larger as the result of increasing EFGs, the quadrupolar coupling cannot be treated as a first-order perturbation on the Zeeman Hamiltonian and second-order contributions to the nuclear spin energies must be determined..

The first order interactions are proportional to C_Q and independent of B_0. The Zeeman energy levels $-m_l$ and m_l are affected equally and the central transition ($\frac{1}{2}$ ↔ $-\frac{1}{2}$) remains as a single line at the isotropic shift. Magic angle spinning (MAS) can be used to remove these first order effects. As C_Q is greater than v_r the satellite transitions are seen as spinning sidebands in the NMR spectra. Second-order interactions are proportional to C_Q^2/v_0 and all the transitions are shifted to different extents. Broadening of line-widths is seen for all transitions, although mainly observed in the central transition as satellite transitions are very difficult to observe if C_Q is large enough for second-order effects to be significant. Unlike first order quadrupolar interactions, second order effects cannot be completely removed by MAS, although, the line-widths are narrowed by a factor of 3 or 4.

Dipolar and J (indirect dipolar) Couplings

Dipolar coupling arises from through-space interactions between the magnetic moments of two nuclei, with the magnitude of the dipolar coupling depending on the distance between the spins and the magnetogyric ratios of the nuclei. J coupling is a corresponding coupling between nuclear magnetic moments occurring through chemical bonding (i.e. via the electrons)   In this thesis the dipolar and J couplings are small in comparison with the shielding and quadrupole interactions and are not considered further.

3.5 Magic Angle Spinning (MAS)

In all materials there is a universal dependence on the applied magnetic field, B_0, and the anisotropic NMR interactions are related to this dependence by $\frac{1}{2}(3cos^2\theta - 1)$. In liquid systems fast tumbling of molecules averages the anisotropic components to zero and the anisotropies in σ and *J* do not affect the resonance frequencies. As a result in solution state NMR very sharp resonances are seen in the spectrum at the average (isotopic) value of the chemical shifts. For solids the anisotropies cannot be ignored as the crystallites are in a fixed orientation to B_0, resulting in broad resonances in the NMR spectrum. MAS is often used in high resolution NMR of powdered samples to reduce the broadening due to anisotropy.

The equation defining shielding involves the term $\frac{1}{2}(3cos^2\theta - 1)$ and in order to simulate isotropic motion in solids, this term must equal to zero. This occurs when θ = 54.74 °. MAS uses this principle and the sample rotor is physically rotated about an axis inclined to 54.74 °, the so-called 'magic angle' (Figure 3.2).
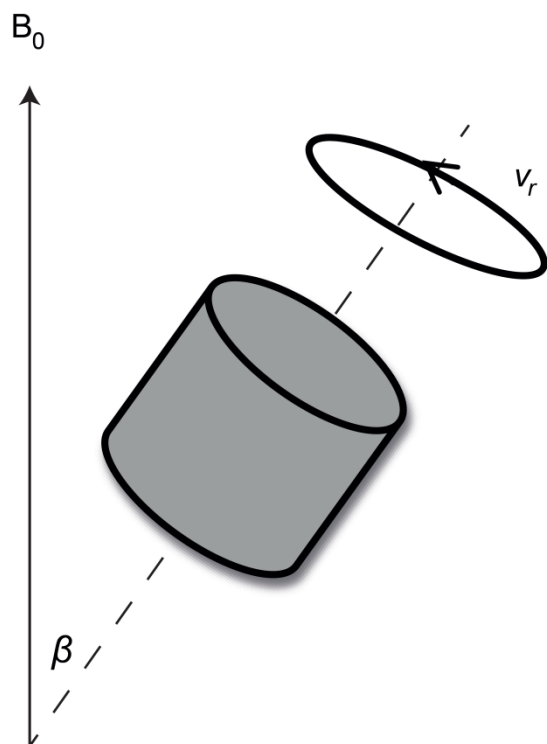
Figure 3.2 Schematic diagram of magic angle spinning experiment. The cylinder represents the spinning sample rotor.

The sample rotor must be spun at a rate greater than or equal to the magnitude of the anisotropic interactions to average them to zero. If the rate is slower, a series of 'spinning sidebands' are observed with a centre-band peak at the isotropic shift position. Varying the spinning speeds can identify the centre-band as the frequency will remain constant and the spinning sidebands will change. The pattern of spinning sidebands is dependent on the anisotropic interactions, and it is possible to extract information such as the quadrupolar anisotropies and asymmetries from the intensity distributions in spinning sideband manifolds using computer programmes (Chapter 6).
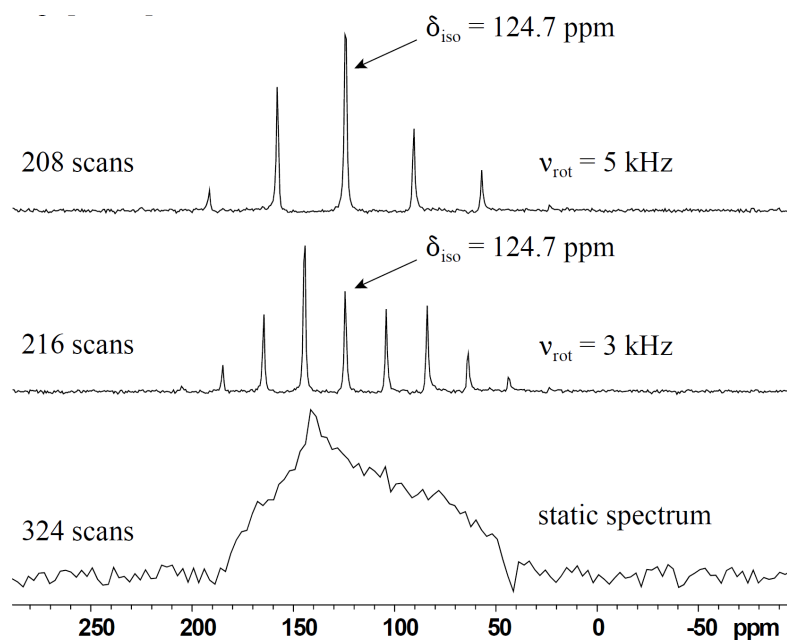
δ_{iso} = 124.7 ppm

208 scans

ν_{rot} = 5 kHz

δ_{iso} = 124.7 ppm

216 scans

ν_{rot} = 3 kHz

static spectrum

324 scans

250   200   150   100   50   0   -50   ppm
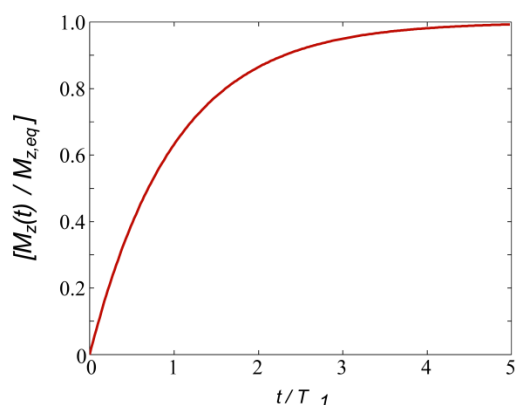
Figure 3.3

3.6 Relaxation

NMR spectra are obtained when NMR sensitive nuclei are placed in an external magnetic field and the response from the bulk spin magnetisation from the radio frequency (RF) radiation as a function of time is recorded (free induction decay, FID). Generally, the external magnetic field is applied in the z plane and the RF tilts the magnetisation towards the *xy* plane. Following a perturbation, spin system returns to thermal equilibrium in a process known as relaxation. There are two major relaxation processes, spin-lattice (longitudinal), T_1, and spin-spin (transverse), T_2 relaxation. T_1 relaxation describes the recovery of the z-component of net magnetisation to the thermal equilibrium and is determined by motion at the NMR frequency. T_1 can be described by:

$$M_z(t) - M_0 = [M_z(0) - M_0]\exp\left(\frac{-t}{T_1}\right)$$

Where:

M_z (0) is the magnetisation in the z direction after perturbation, M_z (t) is the magnetisation in z direction after time t and T_1 is the inverse of fiorst order rate constant for relaxation.

41

Generally, for homogeneous solids, plotting $[M_z(t) / M_{z,eq}]$ as a function of t / T_1 shows and exponential curve (Figure 3.4) and T_1 can be described as a first order rate constant. Values of T_1 can range from seconds to kilo-seconds (diamagnetic samples). T_1 is particularly important in multi-pulse experiments where sufficient time between pulses is needed to allow for spin-lattice relaxation.

Figure 3.4 Graph of $M_z(t) / M_{z, eq}$ as a function of t / T_1 showing the exponential curve and illustrating that T_1 can be described as a first order rate constant.

T_2 relaxation is the relaxation of xy components of magnetisation. In solution-state, T_2 is directly related to line-widths although in solids T_2 is less useful as the line-width due to relaxation is generally negligibly small compared to other line-broadening effects. As relaxation is driven by motion, measurement of relaxation times as a function can provide information on the molecular dynamics of a system.

3.7 CASTEP[49]

CASTEP is a computer code developed by Pickard *et al.*[45,49] which uses Density Functional Theory (DFT) in order to predict the physical properties in materials such as the chemical shift anisotropy (CSA) and electric field gradient tensors (EFG). DFT was developed in 1960's by Walter Kohn, and others, and is a quantum mechanical model which can be used to investigate the electronic structure (mainly the ground state) of atoms, molecules and condensed phases.

It was found that the total energy of a system of electrons in an external potential (in this case the nucleus) is a unique functional of the ground state density. If the density is found, the energy can be calculated. The wave-function is represented by a plane-wave basis set for valence electrons and CASTEP simplifies the representation of this wave-function by using pseudo-potentials to describe the electrons in the core region of the atoms. In the literature this is described by GIPAW[45] (Gauge Including Projector Augmented Wave) method.

In CASTEP, the size of the plane-wave basis set and hence the accuracy of the wave-function description is determined by the cut-off energy. K-point describes the accuracy of the calculations. The quality of this sampling is described by the number of k-points.

Geometry optimisation calculation

The geometry optimisation calculation can provide useful information about a system such as the equilibrium bond lengths and angles; equilibrium cell parameters, discrimination between conflicting structures as well as being the starting point for many advanced investigations. If geometry optimisation calculations were not performed before the NMR parameters were calculated, the resultant NMR parameters gave unrealistic values. In this thesis geometry optimisation calculations were performed before all NMR calculations. In the geometry optimisation calculation, the ground state of a system is found. It is important that the global minimum is found and that the structure does not become stuck in a local minima as this will lead to incorrect structures. The global theoretical minimum can often be different to the experimental minimum as the atomic co-ordinates are optimised. Although, the lattice cell parameters, derived from the X-Ray diffraction, are not optimised (as these are already well defined). Furthermore, DFT calculations are unable to estimate van der waal interactions sufficiently; and the lattice cell parameter values are often underestimated. In this thesis, all lattice cell parameters were fixed. The simplest method of minimising the energy is by steepest descents. This is where the step continues until the local energy starts to rise again whereupon a new direction is selected orthogonal to the previous one

3.8 CASTEP Calculations

The script for inp2cell.py was updated. This converted the TOPAS .inp file to a CASTEP .cell. It also included crystallographic labelling in the CASTEP files.

Previous work, carried out by Anne Soleilhavoup,[50] optimised both the cut-off energy and k-point spacing parameters in order to perform accurate DFT calculations. The cut-off energy relates to the size of the basis set used in DFT and it is important that the correct cut-off energy is used for accurate convergence to occur. It is important the cut-off energy used is optimal with both convergence and processing time. Cut off energies of 900 eV and 1200 eV were used for the geometry optimisation and NMR calculations respectively.

Sampling is also very important in ensuring accurate DFT calculations. This is determined by the number of k-points used in the calculation. It has been shown that the energy of a system is highly dependent on the k-point sampling. The accuracy of the calculation increases with the number of k-points. DFT calculations are carried out in the reciprocal space. The larger the number of points in the sampling the more accurate the calculation is. The sampling is done so by the construction of a grid with spacing between the points (k-point spacing). The larger the unit cell, the smaller the reciprocal space and hence the fewer the number of k-points used. Soliehavoup also carried out calculations to obtain the optimal k-point spacing and it was decided that a k-point spacing of 0.1 $Å^{-1}$ was used to ensure accurate results for both small and larger unit cells.[50]

Preliminary geometry optimisation calculations (for $ZrMo_2O_8$ system) would not converge when using CASTEP default parameters, with the energy of the system oscillated up and down during SCF minimisation rather than smoothly converging. On advice from Stuart Clarke (Physics) the following parameters were used to limit this "charge sloshing". The mix_history_length was changed to 22 from the default value of 7. This parameter determines the maximum number of charge/spin densities to be kept in the mixing history within DM scheme. Mixing_scheme was changed to pulay. The maximum number of conjugate gradient steps that were taken in the electronic minimiser before resetting to the steepest descents direction when doing the band structure calculation was changed from the default value of 25

to 5. With these changes to the parameters, the geometry optimisation calculations converged. Subsequent calculations, on the other systems investigated in this thesis, used these modified parameters.

The parameters used for the geometry optimisation calculation are as follows:
cut_off_energy: 900 eV
functional: PBE

The parameters used for the NMR calculation were the same as previous work.
cut_off_energy: 1200 eV
In both cases the K_POINT_SPACING used was 0.1.

Figure 3.5 shows the parameters used in both the geometry optimisation and NMR calculations in this report.

```
task : GeometryOptimization        task : MagRes
cut_off_energy : 600 eV            magres_task : NMR
xc_functional : PBE               cut_off_energy : 1200 eV
opt_strategy : speed              xc_functional : PBE
num_backup_iter : 10              opt_strategy : speed
geom_max_iter : 100               max_scf_cycles : 100
max_scf_cycles : 150              mix_history_length : 22
mix_history_length : 22           mixing_scheme : pulay
mixing_scheme : pulay             iprint : 2
iprint : 1
```

Figure 3.5 Examples of the .param file used for the geometry optimization and NMR calculations.

A magres file is created by CASTEP which contains all the NMR parameters which have been calculated. This magres file is converted to an .inc file using magres2pNMRsim[51] using in-house software. This .inc file was then used to create predicted spectra. The shifts, spinning speed and magnetic field (B_o) were all defined and hence spectra could be simulated for different speeds and different magnetic fields. This is advantageous as experimental and predicted spectra could be compared. The spectra were simulated using GDIS[52].

Chapter 3 Experimental

3.1 Preparation of $ZrMo_2O_7(OH)_2.2H_2O$

Perchloric acid and hydrochloric acid were used as two different routes to synthesise the precursor. This method involves the reflux of the reagents solutions in either of the acids. Previous methods of synthesis involving hydrothermal bombs were not successful.

Synthesis using perchloric acid

In separate beakers 1.77 g of $(NH_4)_6Mo_7O_{24}.4H_2O$ (9.0 mmol, Alfa Aesar) and 2.2515 g of $(ZrO(ClO_4)_2.8H_2O$ (5.0 mmol, Aldrich) were dissolved in deionised water (30 cm^3) to form colourless solutions. The two solutions were added dropwise with continuous stirring. An off white / light grey precipitate immediately formed. The solution was stirred for several hours at room temperature. 80 cm^3 of perchloric acid (Sigma Aldrich, 70%) was added to the solution and was refluxed for 3 days at 150 ^{o}C. The solution was cooled and the grey precipitate was washed with deionised water and centrifuged. This was repeated until the washings were approximately pH 7. The grey precipitate (RKY013 and JER100 and JER113) was then dried in a hydrothermal oven at 100 ^{o}C. PXRD was used to confirm that the grey precipitate was the precursor.

Synthesis using hydrochloric acid

The above method was repeated, using 80 cm^3 of hydrochloric acid (Fisher Scientifica) in the reflux step.

3.2 Preparation of samples for PXRD

VT XRD

A sample of $ZrMo_2O_7(OH_2).2H_2O$ was prepared for VTXRD by grinding the powder in an agate pestle and mortar and sprinkling though an 80 mesh sieve onto an amorphous SiO_2 disc greased with Vaseline. Any excess powder was tapped off and the process was repeated until there was sufficient coverage of the sample on

the SiO_2 disc. Continuous scans were run as the HTK 1200 furnace was heated at a rate of 2 K min^{-1} with a step size of 0.02 K.

Ambient temperature XRD

A sample of compound was prepared by grinding the solid in an agate pestle and mortar and placed onto a bulk sample holder. The samples were scanned from 10° to 70° 2θ using Siemens d5000 Powder Diffractometer at ambient temperature. The recorded data were analysed using TOPAS Academic.

3.3 Preparation of samples for Scanning Electron Microscopy

The sample was ground in an agate pestle and mortar and sprinkled though an 80 mesh sieve onto a carbon disc. The samples were coated with 35 nm of platinum. SEM images were collected on Hitachi SU70 SEM.

3.4 Preparation of cubic $ZrMo_2O_8$

Cubic $ZrMo_2O_8$ was prepared by the method developed by Allen[3]. Perchloric acid derived $ZrMo_2O_7(OH)_2.2H_2O$ was placed into the furnace and heated at a heating rate of 2 Kmin^{-1} for 30 minutes. The sample was rapidly quenched in air, reground and placed back into the furnace for a further 15 minutes. The sample was taken out of the furnace, ground and XRD pattern was recorded.

3.5 Preparation of amorphous $SnMo_2O_8$

The co-precipitation synthesis used by Buiten has been developed and improved by Feja and Fall. The co-precipitation method used in to obtain the optimum sample of $SnMo_2O_8$ in this thesis was perfomed by Child and Tallentire.

2.1046 g of $SnCl_4.5H_2O$ (Aldrich, 98 %) was dissolved in 12 cm^3 of deionised water to form a colourless solution. 2.11 g of $(NH_4)_6Mo_7O_{24}.4.89H_2O$ (Alfa Aesar, 99.9999%) was dissolved in 12 cm^3 of distilled water. The two solutions were added drop-wise into 6 cm^3 of deionised water with continuous stirring. An off-white precipitate immediately formed. This solution was stirred overnight. The precipitate

was separated by filtration and dried in an oven at 323 K. PXRD confirmed the off white solid (RKY028) to be amorphous.

Preparation of cubic SnMo$_2$O$_8$

Child optimised the synthesis conditions to prepare cubic SnMo$_2$O$_8$. In a furnace, amorphous SnMo$_2$O$_8$ was heated to 863 K with a heating rate of 5 K min^{-1} and left to dwell at this temperature for 30 minutes. PXRD confirmed cubic SnMo$_2$O$_8$ had been formed (Figure 3.1).
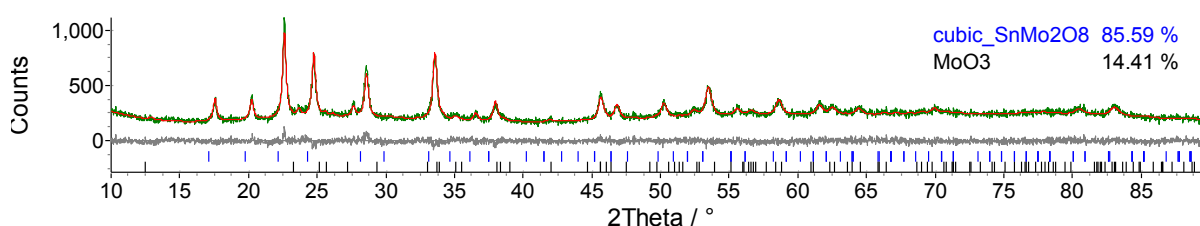
Figure 3.1 Rietveld refinement of XRD data for ^{17}O enriched SnMo$_2$O$_8$ (d7_01849, R$_{wp}$ 11.650 %). Bragg peak positions are shown by tick marks for cubic SnMo$_2$O$_9$ (blue), MoO$_3$ (green).and SnO$_2$ (green).

3.6 ^{17}O enrichment of SnMo$_2$O$_8$

The glassware used for the ^{17}O enrichment of SnMo$_2$O$_8$ was designed by Child and Tallentire and custom built as shown in Figure 3.2. The specification for the design was based on the amount of ^{17}O at 0.5 atm at room temperature required to obtain 20% enrichment. All the glassware was made of glass except the quartz boat (holds the reagent). The tube has an external and internal diameter of 22 mm and 15 mm respectively.   The pressure of the system was monitored using a Baratron (measures from 0 to 1000 Torr) connected to a voltmeter. It is the voltage which is monitored and the relationship between voltage and pressure is shown in Table 3.1. Any reduce 'dead' volume a glass rod was placed between the Baratron and tube. The ^{17}O$_2$ gas used was 60 % enriched in a 460 ml Aldrich lecture bottle with a pressure of 2.38 atm.
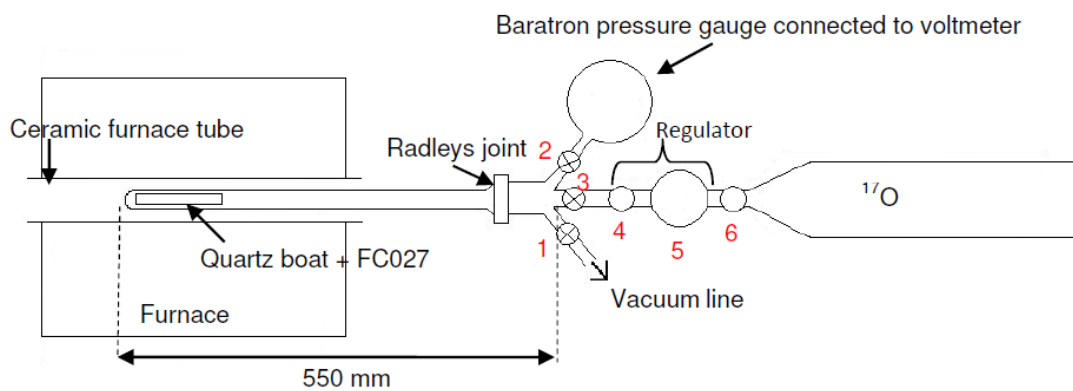
Figure 3.2 Experimental set up for ^{17}O gas exchange enrichment method as developed by Tallentire and Child.

Voltage / V	Pressure / Torr	Pressure / atm	Pressure / mbar
1.0×10^{-4}	0.01	1.32×10^{-5}	0.01333
5.0×10^{-4}	0.05	6.58×10^{-5}	0.06667
1.0×10^{-3}	0.10	1.32×10^{-4}	0.1333
5.0×10^{-3}	0.50	6.58×10^{-4}	0.6666
1.0×10^{-2}	1.0	1.32×10^{-3}	1.333
0.5×10^{-2}	5.0	6.58×10^{-3}	6.666
0.1	10	1.32×10^{-2}	13.33
0.5	50	6.58×10^{-2}	66.66
1.0	100	0.132	133.3
1.5	150	0.197	200
2.0	200	0.263	266.6
2.5	250	0.329	333.3
3.0	300	0.395	400.0
3.5	350	0.461	466.6
4.0	400	0.526	533.3
4.5	450	0.592	600.0
5.0	500	0.658	666.6
6.0	600	0.789	799.9
7.0	700	0.921	933.3
8.0	800	1.053	1067
9.0	900	1.184	1200
10.0	1000	1.316	1333

Table 3.1 Relationship between voltage and pressure (in Torr, atmosphere and mbar).

^{17}O enrichment of cubic SnMo$_2$O$_8$ procedure 1

0.5017 g of LT cubic $SnMo_2O_8$ (FC027) was ground finely in an agate pestle and mortar. The sample was placed into the quartz boat and inserted to the end of the glass tube. As the equipment is non-standard and designed in-house, its operation is described in detail here. Vacuum grease was used on all joints to ensure a complete vacuum. Apart from the Radley's joint, jubilee clips were used to secure all other joints. To ensure only $^{17}O_2$ gas was present during the enrichment, the entire

system was evacuated using a vacuum pump and line. Systematic evacuation of air of each part of the apparatus was needed to ensure the material in the quartz boat was not affected. Initially only tap 1(only the tube was evacuated) was opened, followed by tap 2 (to the Baratron). Tap 3 was opened so all glassware was under a vacuum, but the regulator valves were shut. Voltage and vacuum line readings at each point of evacuation were noted to monitor the pressure (Table 3.2). Taps 1 and 3 were closed to isolate the tube, (at this point the vacuum pump can be turned off). Tap 6 (on the regulator) was opened to allow $^{17}O_2$ gas from the cylinder into the regulator. Valve 5, which controls the pressure gauge in the regulator, was opened until the desired pressure was achieved. Tap 6 was closed (shutting off the $^{17}O_2$ gas supply) and valve 4 was opened. Tap 3 was opened slowly to control the introduction of $^{17}O_2$ into the tube to ensure the no material was disturbed. Transfer of $^{17}O_2$ gas was completed in stages. After the initial transfer, the voltage reading was noted. Tap 3, 4 and 5 were closed, tap 6 was opened and the procedure was repeated until the desired pressure in the tube had been achieved. Once at the desired pressure, taps 3, 4 and 5 were left open and liquid N_2 was used to cool the end of the tube in order to condense as much $^{17}O_2$ gas left in the regulator, minimising waste. Voltage before and after cooling was noted. Once glass tube was warmed to room temperature a ceramic tube was placed around it and inserted into a tube furnace.

	Pressure Sensor (vacuum line) / x 10^{-1} mbar	Voltage / V	Pressure / atm (in the system)	Regulator pressure / atm
Initial under vacuum	6.4			
Line to tube open	7.8			
Line to baratron open	7.8	0.189	0.0249	
after glassware	7.6	19.4	2.553	
open but not regulator				
Taps 3,4 & 5 open	7.4	0.0194	0.00255	
Taps 6 then 5 open	6.8	0.0209	0.00275	
1st transfer ^{17}O		1.91	0.251	0.6
2nd transfer ^{17}O		3.45	0.454	0.6
3rd transfer ^{17}O		4.78	0.629	0.4
4th transfer ^{17}O		5.74	0.755	0.4
Liquid nitrogen		5.25	0.691	
Warming up after liquid nitrogen		6.27	0.825	

Table 3.2 The pressure and voltage obtained during the evacuation of the experimental set up (Figure 3.2) and the subsequent introduction of ^{17}O gas into the glass tube. These values were used as a reference for subsequent ^{17}O enrichments.

The furnace was set to 773 K. Temperatures and Baratron readings were monitored until 500 ^{o}C (Table 3.3) and tap 3 was closed off to the Baratron and the system was left at 500 ^{o}C for 24 hours. A second enrichment was carried out with the sample being ground briefly between enrichments. The readings were monitored as before. This enrichment process was left for 3 days. ^{17}O NMR of the sample was carried out as described in detail in Chapters 4-6**.**

Temperature / °C	Voltage / V	Pressure / atm
25	6.27	0.825
104	6.57	0.864
204	6.97	0.917
350	7.46	0.982
400	7.48	0.984
450	7.51	0.988
550	7.60	1.00

Table 3.3 The voltage and pressure as the system is heated to 550 °C in a tube furnace.

^{17}O enrichment of $SnMo_2O_8$ procedure 2

An alternative enrichment method was to use the same procedure as explained above but using amorphous $SnMo_2O_8$ (0.543 g) instead of LT cubic $SnMo_2O_8$. The furnace was heated to 550 °C with a heating rate of 2 °C min^{-1} and held for 5 days. The glass tube was removed from the furnace and quickly cooled. PXRD was collected (Figure 3.3) and shows that cubic phase had been formed in the furnace.
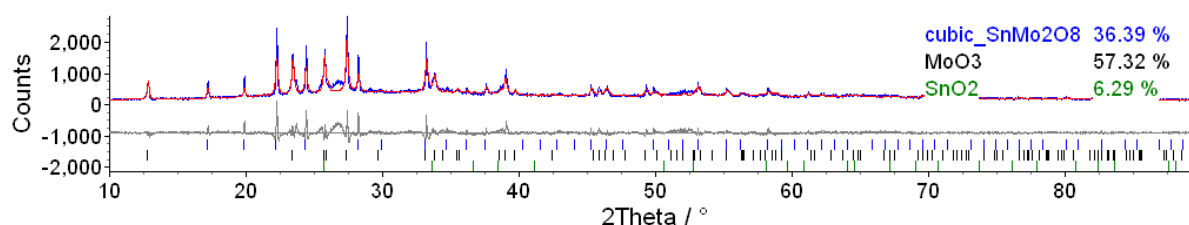
Figure 3.3 Rietveld refinement of XRD data for ^{17}O enriched $SnMo_2O_8$ (d7_01849, R_{wp} 11.650 %). Bragg peak positions are shown by tick marks for cubic $SnMo_2O_9$ (blue), MoO_3 (green).and SnO_2 (green).

^{17}O enrichment of cubic $ZrMo_2O_8$

The enrichment procedure used was the same as $SnMo_2O_8$ with 0.8 atm of ^{17}O gas used in one enrichment. ~ 0.5 g of cubic $ZrMo_2O_8$ (section 3.4) was placed into the quartz boat. All the readings were monitored as before and the system was left for 2 weeks. PXRD and ^{17}O NMR were used to characterise the solid.

3.7 NMR experiments

Current high field NMR spectrometers use the principle of Fourier Transform (FT) NMR. A sample is held in a static magnetic field (B_0) while short pulses (typically with a duration of 1 – 100 µs) of resonant radiofrequency radiation are applied to excite a range of frequencies centred at the NMR frequency of interest. After excitation the magnetisation precesses in the *xy* plane. This oscillating magnetic field generates the NMR signal, often called the free induction decay (FID). This FID can then be Fourier transformed to give a frequency spectrum.

Most of the experiments were performed on a 500 MHz Varian InfinityPlus spectrometer. Additional experiments carried through the Durham Solid-State NMR Service (400 MHz Varian VNMRS spectrometer) and the 850 MHz National Facility (850 MHz Bruker Avance Spectrometer).

Single Pulse Experiment

The pulse sequence used to record an NMR spectrum using a single pulse is shown in Figure 3.4. This is the simplest experiment and the spins are excited at the Lamor frequency using a hard pulse. The receiver is then turned on to acquire the FID.

The FID is at a maximum when the spin flip angle is equal to 90°. This 90° pulse width, τ_{90}, can be calibrated using a pulse width array. The maximum signal will be when τ is equal to τ_{90} and zero when τ is equal to τ_{180}.
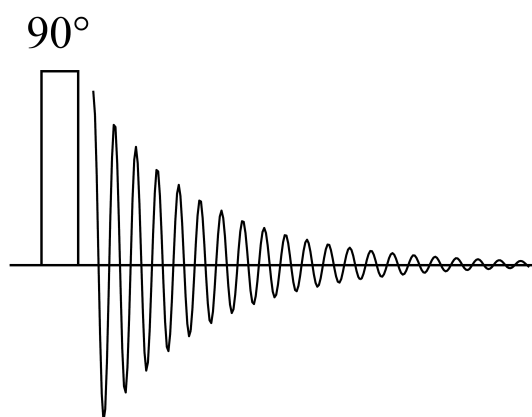
Figure 3.4 Pulse sequence for single pulse NMR experiment

Solid Echo Experiment

Broad signals caused by quadrupolar interactions result in rapidly decaying free induction decays. In these cases a significant fraction of the FID is lost / distorted due to 'dead time' between the end of the pulse and start of acquisition. This results in loss of signal intensity and spectral distortion. In this project static echo experiments were performed to overcome this problem. These experiments involved applying a 90° pulse; waiting for a period of time, τ, and then another 90° pulse was applied. After another period of τ, the signal was refocused and signal acquired. Figure 3.5 shows the pulse sequence.

$$(90°)_x \qquad (90°)_y$$
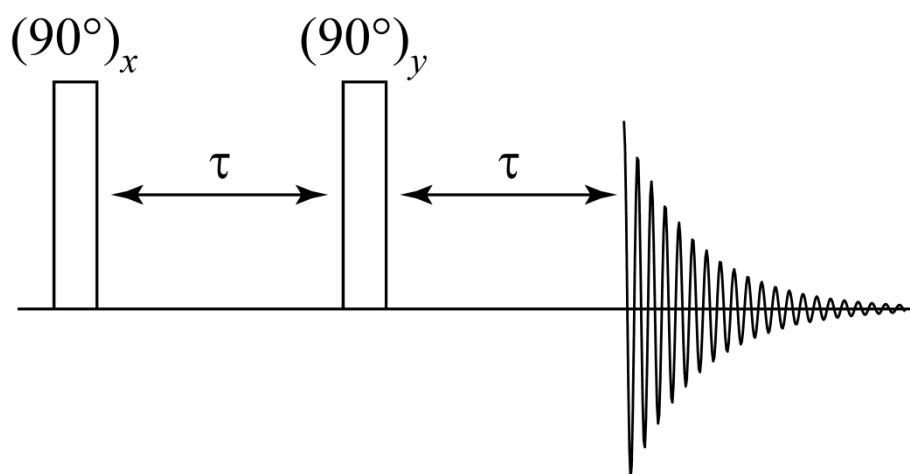
Figure 3.5 Pulse sequence used for solid-echo NMR experiments.

Quadrupolar Carr-Purcell Meiboom-Gill (QCPMG) Experiment

QCPMG can be used for the rapid acquisition of solid-state NMR spectra of half-integer quadrupolar nuclei, which are broadened by second-order quadrupolar interactions (where magic-angle spinning is only partially useful). This experiment starts with excitation followed by a series of π pulses with acquisition of the echo after each π pulse (Figure 3.6). The echoes are Fourier transformed to give a series of equally spaced sharp "spikelets" outlining static powder patterns. The advantage of this experiment over the standard quadrupolar-echo experiment is that the broad signals from second-order powder patterns are refocused by the π pulses allowed many echoes to be acquired before the NMR signal decays due to relaxation. Hence the resulting spectra have much better signal-to-noise than corresponding static

55

(quadrupolar) echo experiments carried out in the same time. In this project QCMPG experiments were carried out to obtain initial ^{87}Rb and ^{93}Nb spectra and high better quality static-echo experiments were performed in order to observe well-defined second-order line-shapes.
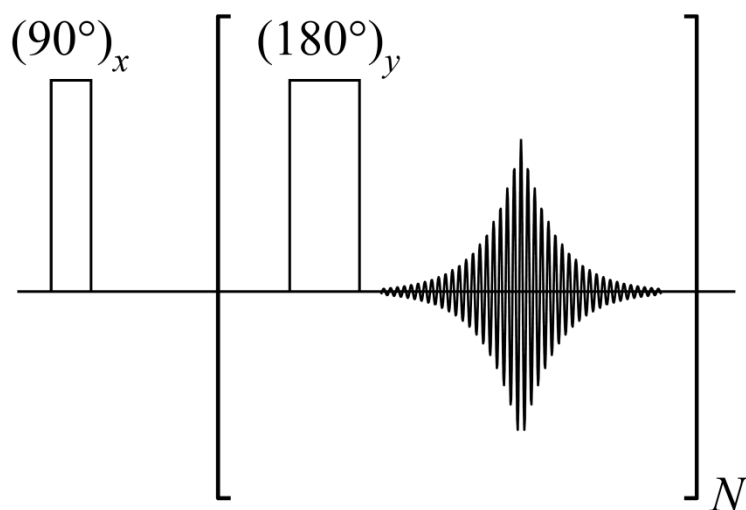

Figure 3.6 Pulse sequence used for QCPMG experiments.

Chapter 4 Preparation and Characterisation of Cubic Zirconium Molybdate

Lind *et al.*[24] first prepared and reported cubic $ZrMo_2O_8$ as a pure phase in 1998 from the dehydration of the precursor, $ZrMo_2O_7(OH)_2.2H_2O$. The precursor was characterised by Clearfield and Blessing[53] in 1972. This chapter describes the preparation of $ZrMo_2O_7(OH_2).2H_2O$, LT-$ZrMo_2O_8$, cubic $ZrMo_2O_8$ and trigonal $ZrMo_2O_8$ phases by a low temperature topotactic route; and the characterisation of these phases using powder X-ray diffraction (PXRD) and Scanning Electron Microscopy (SEM). The aim was to identify conditions in which [17]O enriched cubic $ZrMo_2O_8$ could be prepared for solid state NMR. The particle size for each of phases was obtained from perchloric acid and hydrochloric acid derived compounds. The impact of this parameter on the isolation of cubic-$ZrMo_2O_8$ will be discussed.

4.1 Rietveld Analysis

Synthesis and in-situ variable temperature (VT) XRD of $ZrMo_2O_7(OH_2).2H_2O$

In-situ VT XRD data was collected using the groups Bruker d8 and d9 diffractometers using a HTK 1200 high temperature furnace (Chapter 2). Data were collected in 39 steps with 19 minute scans, with a 2 K min^{-1} ramp rate between temperatures and a 2θ range of $10 - 70^{o}$. The samples were prepared for VT XRD as described in Chapter 3. As structural models of the four phases of zirconium molydate encountered have been previously obtained, Rietveld analysis of both perchloric and hydrochloric acid derived $ZrMO_2O_7(OH_2).2H_2O$ could be used to determine the fraction of each phase at each temperature.

A TOPAS[54] seed file was set up including the structural models for the four phases and ZrO_2, along with the Rietveld refinement parameters for each phase. A total of 39 parameters were refined. These included a height parameter, 12 co-efficients of Chebyshev polynomial to model the background and three parameters to describe a Pseudo-Voigt peak (peak position, intensity and full width half maximum) to model diffraction from the furnace window. The fwhm was contrained with limits of 1 to 6 such that the peak remained broad and could not refine to fit a sharp Bragg

reflection. For all phases 1 scale factor, 1 isotropic thermal displacement parameter and crystallite size (L_{vol}) were refined. The required distinct lattice parameters for each space group for each phase were refined.

LT $ZrMo_2O_8$ is hard to model due to large strain broadening being present. From VT XRD data where the LT phase is the dominant phase, the spherical harmonics were refined to fit experimental peaks and then fixed and all subsequent refinements were performed with these parameters.

The refined phase fractions can be taken from the Rietveld refinements of VT XRD data and the temperature dependence of each phase is shown in Figure 4.1 . A temperature calibration had to be applied to the VT XRD temperatures. This was obtained by Allen and Equation 4.1 was used to obtain the actual temperature in the Anton Parr HTK 1200 furnace[3].

$$T_{corr} = T + aT^3 + bT^2 + cT + d \qquad \text{Equation 4.1}$$

Where:

a = 1.61 x 10^{-7} K^{-2}

b = -5.86 x 10^{-4} K^{-1}

c = 0.565

d = -134 K

Figure 4.1 shows the phase evolution on heating perchloric acid derived $ZrMo_2O_7(OH)_2.2H_2O$ (sample ID JER 100). The precursor starts to dehydrate to LT $ZrMo_2O_8$ at 390 K. The formation of cubic $ZrMo_2O_8$ also begins during this temperature range, however, at 616 K LT $ZrMO_2O_8$ starts to disappear and cubic $ZrMo_2O_8$ is formed. In this sample, cubic $ZrMo_2O_8$ is present phase-pure between 650 and 720 K. After 720 K, cubic $ZrMo_2O_8$ is no longer stable and slowly starts to converts to trigonal $ZrMo_2O_8$. At 779 K, approximately 50-50 % trigonal and cubic $ZrMo_2O_8$ is present. Above 900 K, the decomposition to binary oxides occurs.
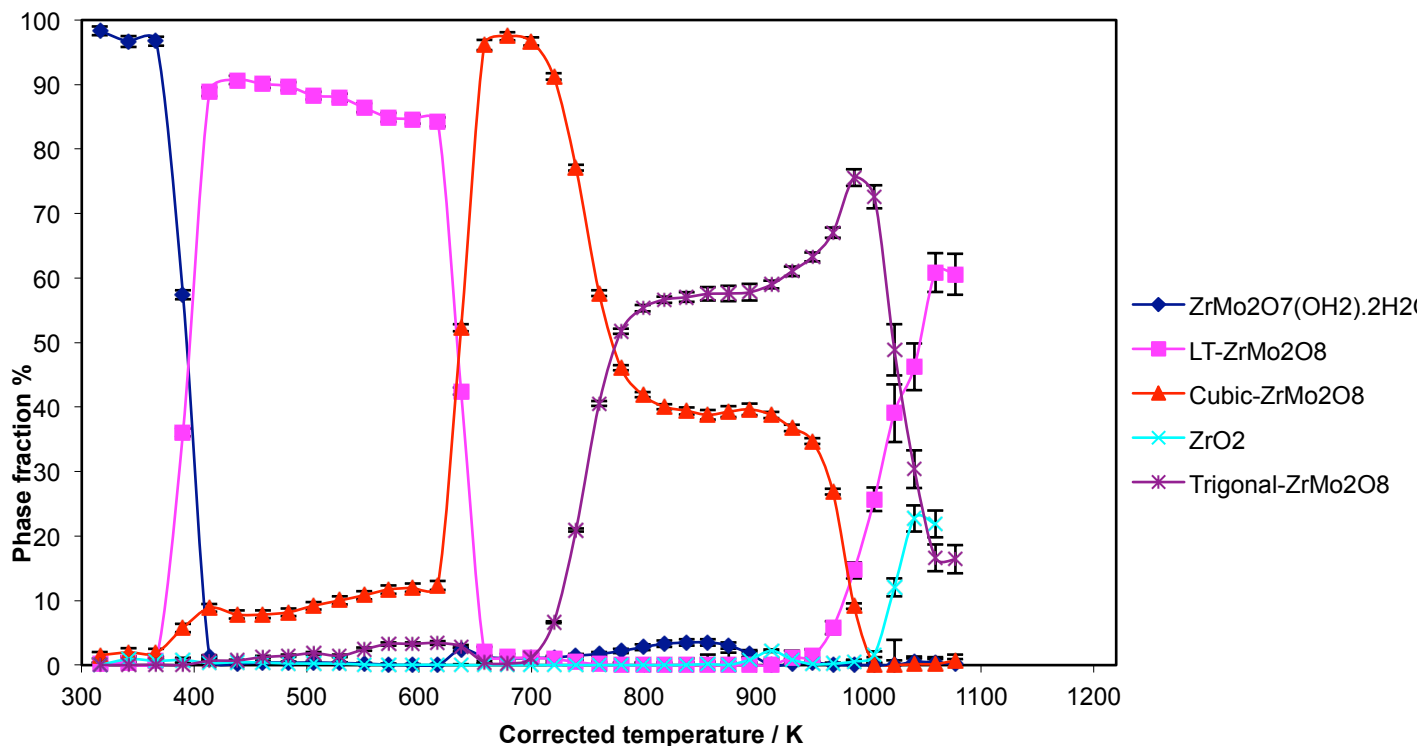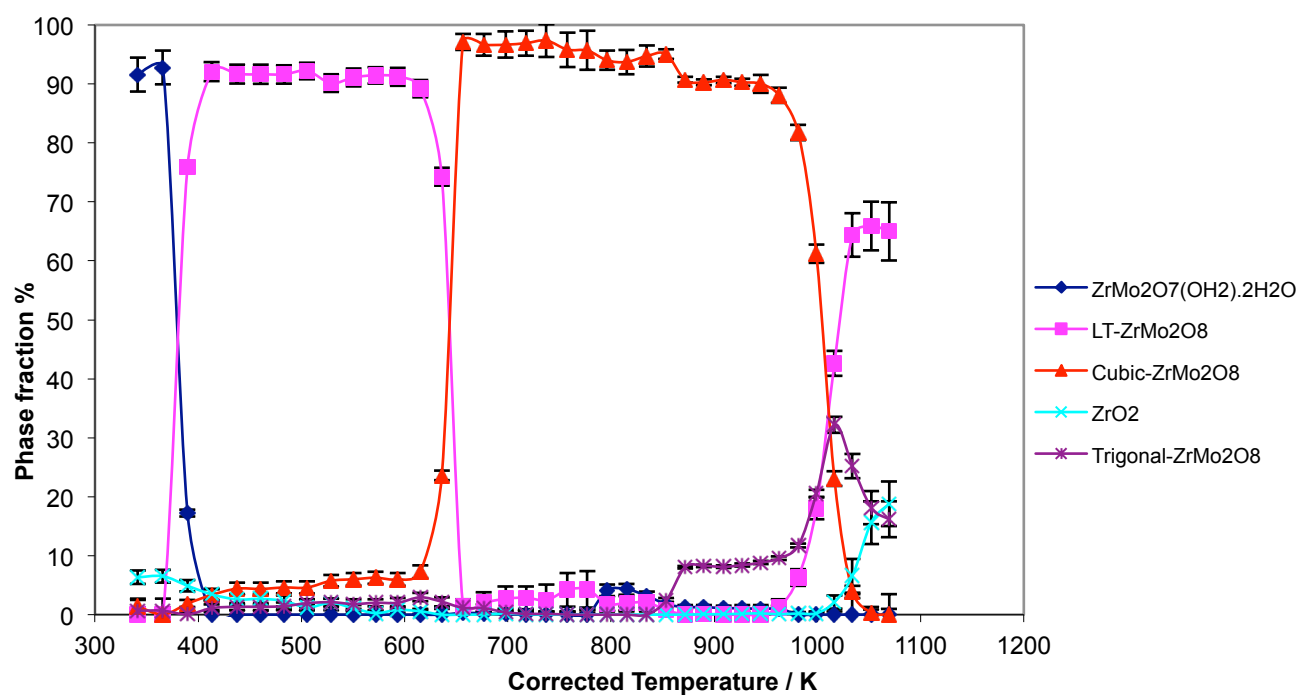
Figure 4.1 Percentage composition as a function of temperature for variable temperature powder X-ray diffraction experiments on $ZrMo_2O_7(OH)_2.2H_2O$ (JER 100, experiment code d8_04015).

The temperature dependence graphs of each sample highlight the difficulties of the synthesis of phase-pure cubic $ZrMo_2O_8$, even when the starting reagents are the same. All perchloric acid derived $ZrMo_2O_7(OH)_2.2H_2O$ samples (JER 100, JER 113 and RKY 013) behave slightly differently and the quantitative VT XRD results are different (*e.g.* Figure 4.2 and Figure 4.3). Perchloric acid derived $ZrMo_2O_7(OH)_2.2H_2O$ (JER 113) shows cubic $ZrMo_2O_8$ is phase pure between 650 and 850 K and slow conversion to trigonal $ZrMo_2O_8$ occurs at temperatures higher than 850 K. Decomposition to the binary oxides occurs at temperatures greater than 1000 K. RKY 013, however, shows surprising results. LT $ZrMo_2O_8$ is present to slightly higher temperatures. Cubic $ZrMo_2O_8$ is also phase pure for a much larger temperature range, ~ 700 to 1000 K. These VT XRD results show that this was the best sample from which prepare [17]O enriched cubic $ZrMo_2O_8$.
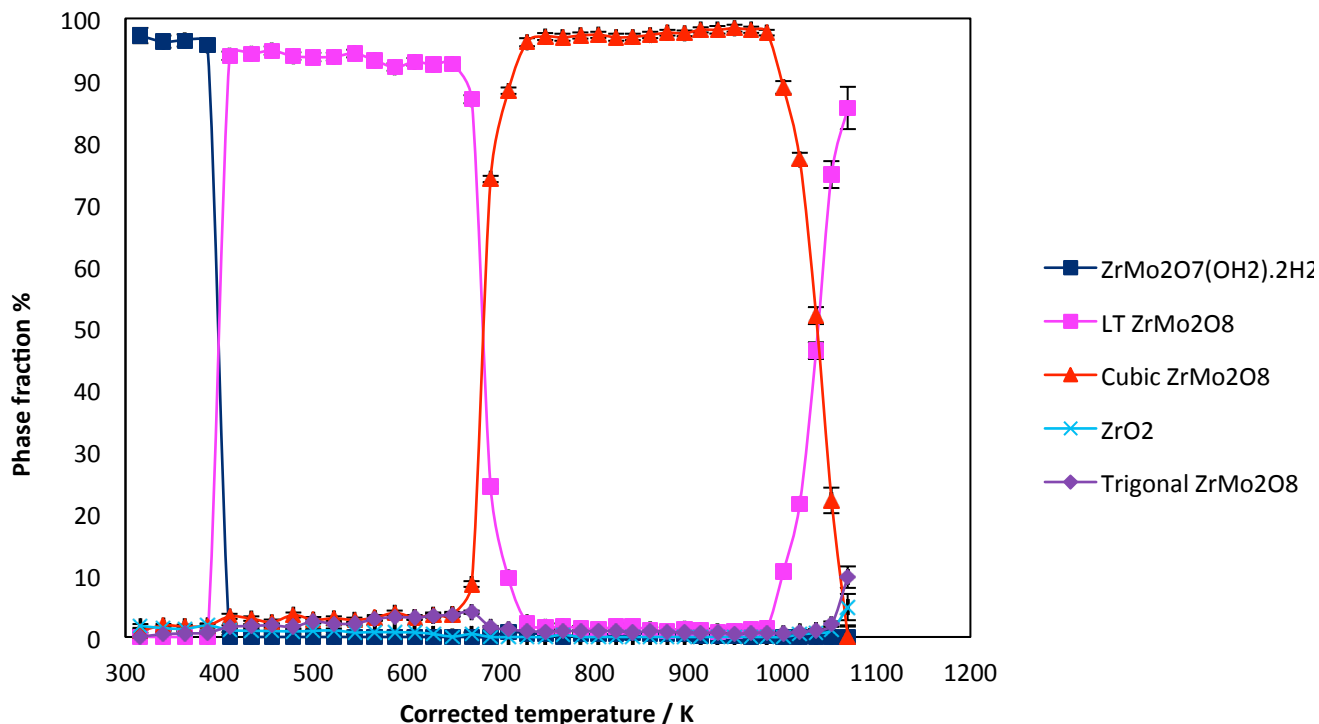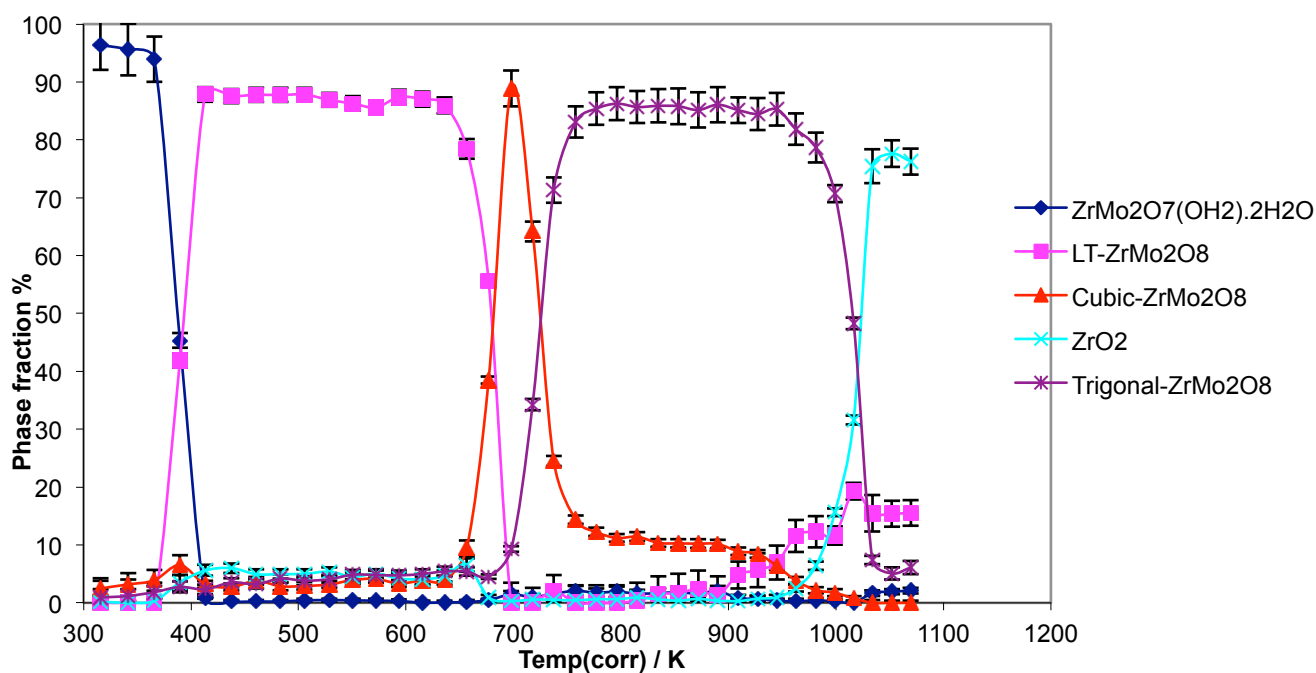
Figure 4.2 Percentage composition as a function of temperature for variable temperature powder X-ray diffraction experiments on perchloric acid derived ZrMo$_2$O$_7$(OH)$_2$.2H$_2$O (JER 113, experiment code d9_04487).
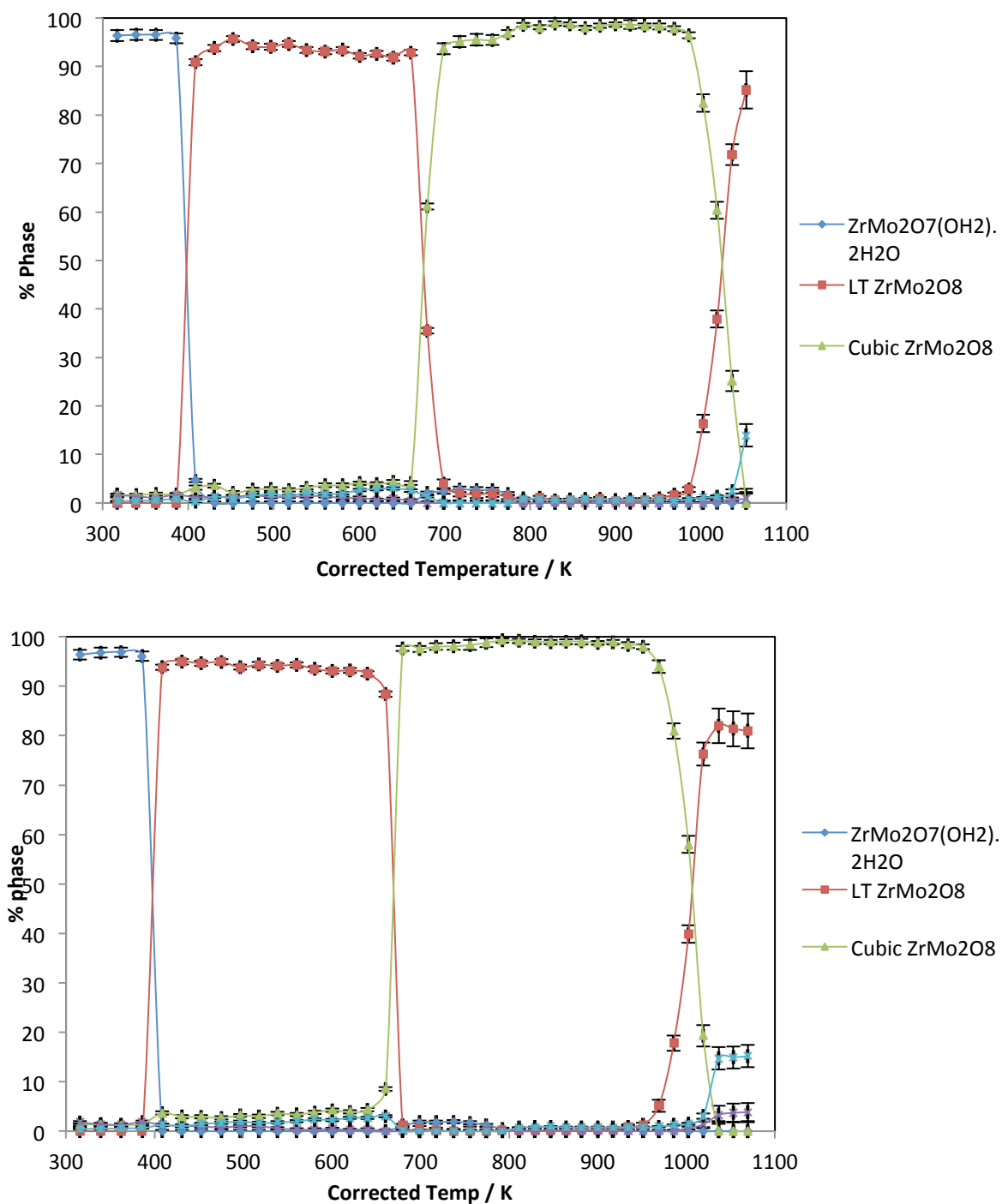
Figure 4.3 Percentage composition as a function of temperature for variable temperature powder X-ray diffraction experiments on perchloric acid derived ZrMo₂O₇(OH)₂.2H₂O (RKY013, experiment code d9_06435).

In comparison, the hydrochloric acid derived $ZrMo_2O_7(OH)_2.2H_2O$ (sample ID JER 122), LT $ZrMo_2O_8$ starts to convert to cubic $ZrMo_2O_8$ at 656 K. Cubic $ZrMo_2O_8$ is not present phase-pure as trigonal $ZrMo_2O_8$ is always present, albeit in very small quantities. Cubic $ZrMo_2O_8$ is present with very small quantities of trigonal $ZrMo_2O_8$ between 697 and 717 K. This temperature range is much smaller than in perchloric acid derived precursor. After 700 K the more thermodynamically stable trigonal polymorph is formed. This method of synthesis is not useful in the preparation of cubic $ZrMo_2O_8$.

Figure 4.4 Percentage composition as a function of temperature for variable temperature powder X-ray diffraction experiments on hydrochloric derived $ZrMo_2O_7(OH)_2.2H_2O$ (JER 122, experiment code d9_04493).

Investigation into the length of scan time at each temperature in VT XRD, and hence the length of time the sample is held at each temperature, showed that this did not affect the temperatures at which LT $ZrMo_2O_8$ is present (Figure 4.5). The scan time of 20 minutes was used in subsequent VT XRD experiments.

Figure 4.5 Percentage composition as a function of temperature for variable temperature powder X-ray diffraction experiments on perchloric derived ZrMo₂O₇(OH)₂.2H₂O (RKY 013), for scanning time of 30 minutes (top, d9_06437) and 50 minutes (bottom, d9_06441).

As with Lind *et al.*[24], (Chapter 1) these quantitative XRD results show the importance of the starting reagents and how they affect the thermal evolution behaviour of the precursor, $ZrMo_2O_7(OH)_2.2H_2O$. Further investigation into particle size from VT

XRD, ambient temperature XRD and Scanning Electron Microscopy (SEM) provides insight into why this behaviour is observed and when formation of phase pure cubic $ZrMo_2O_8$ (section 4.2) is possible.

Ambient temperature XRD

From VT XRD data, key temperatures were chosen, 723 K, 823 K and 923 K, to prepare bulk samples of zirconium molybdate to obtain more XRD data to learn more about the microstructure of the various phases. These temperatures were chosen from VT XRD data as phase pure cubic $ZrMo_2O_8$ is present at 723 K, a mixture of cubic and trigonal $ZrMo_2O_8$ at 823 K and phase-pure trigonal $ZrMo_2O_8$ at 923 K. Samples were prepared by *ex-situ* heating in a muffle furnace using a ramp rate of 10 K min^{-1} and then cooled at the rate at which the furnace cools. The samples were prepared for VT XRD as described in Chapter 3.

The structural models of each phase for the ambient temperature XRD were the same as those used in VT XRD analysis. A total of 41 parameters were refined, including 19 background parameters, a simple axial model to model the asymmetry, a height parameter, 8 spherical harmonic parameters (modelling preferred orientation), 1 scale factor, 1 isotropic thermal displacement parameter equated for all atoms, 2 lattice parameters, 6 *xyz* fractional atomic coordinate parameters for 2 Mo atoms and a partial occupancy parameter. More background parameters were used in comparison to VT XRD to improve the refinement and reduce the R_{wp} values. Figure 4.6 to Figure 4.7 show the Rietveld refinements of the XRD data for perchloric acid derived phases (JER 100 and JER 113) and chloride derived phases (JER 122). Comparison of JER 100 and JER 113 with the Rietveld refinements of VT XRD data show that when the precursor is furnace-heated to 723 K, a mixture of cubic and trigonal $ZrMo_2O_8$ is present (JER 100, 73.41:24.73 and JER 113). The *in-situ* VT XRD Rietveld refinements show that at this temperature for both these samples, cubic $ZrMo_2O_8$ should be the only phase present (Figure 4.1 and Figure 4.2). Chloride derived precursor heated to 723K *ex-situ* only has trigonal $ZrMo_2O_8$ present and also disagrees with VT XRD data, which suggests that at this temperature, some cubic $ZrMo_2O_8$ should be present. This suggests that producing phase pure cubic $ZrMo_2O_8$ is dependent on the heating rates.

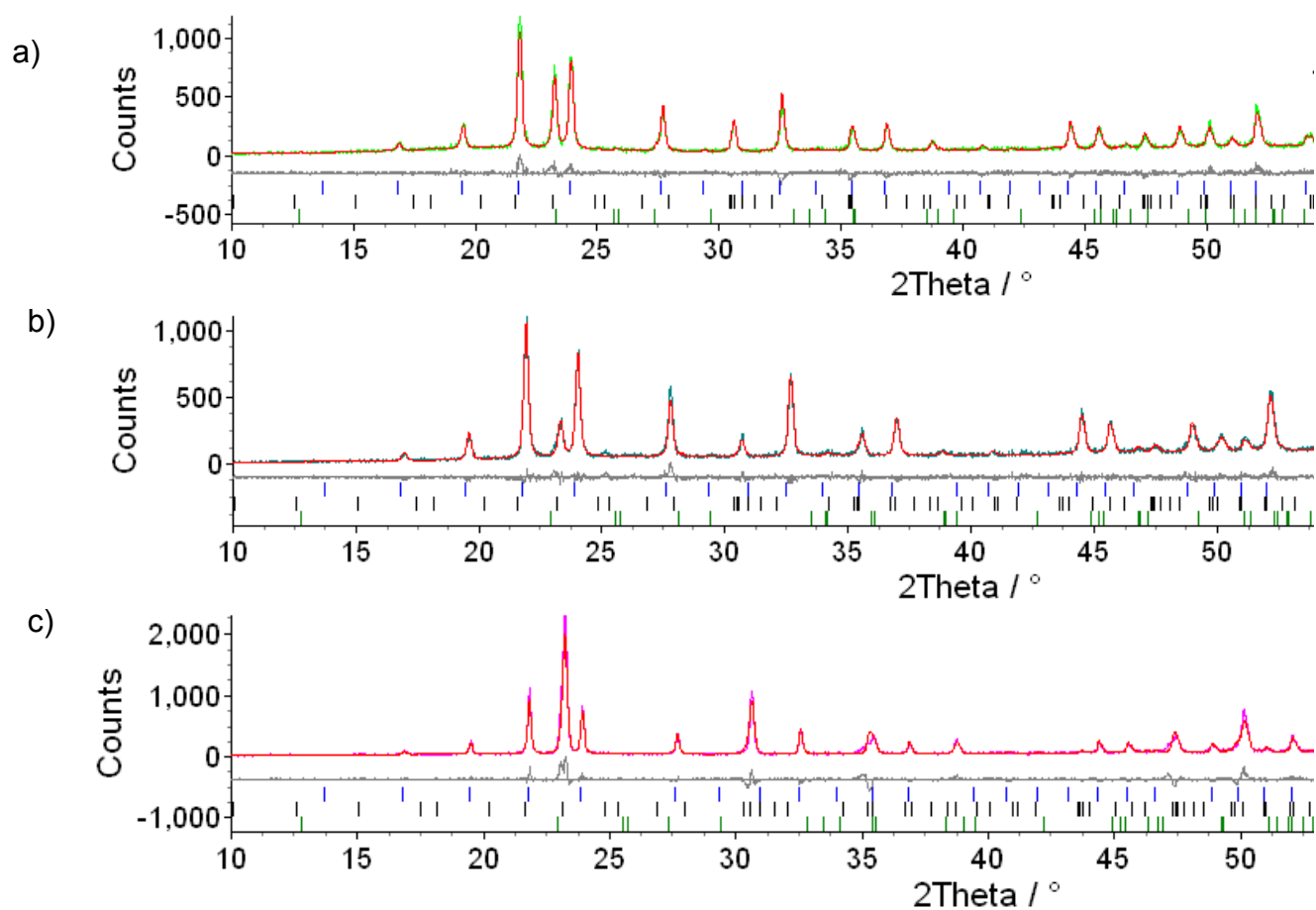**Figure 4.6 Rietveld refinement of XRD data for ZrMo$_2$O$_8$ heated to 723 K *ex-situ* a) JER 100_723 (d5_09528, R$_{wp}$ 12.692 %), b) JER 113_723, (d5_09535, R$_{wp}$ 11.466 %) and c) (d5_09553, R$_{wp}$ 17.531 %). Bragg peak positions are shown by tick marks for cubic ZrMo$_2$O$_9$ (blue), trigonal ZrMo$_2$O$_8$ (black) and MoO$_3$ (green).**
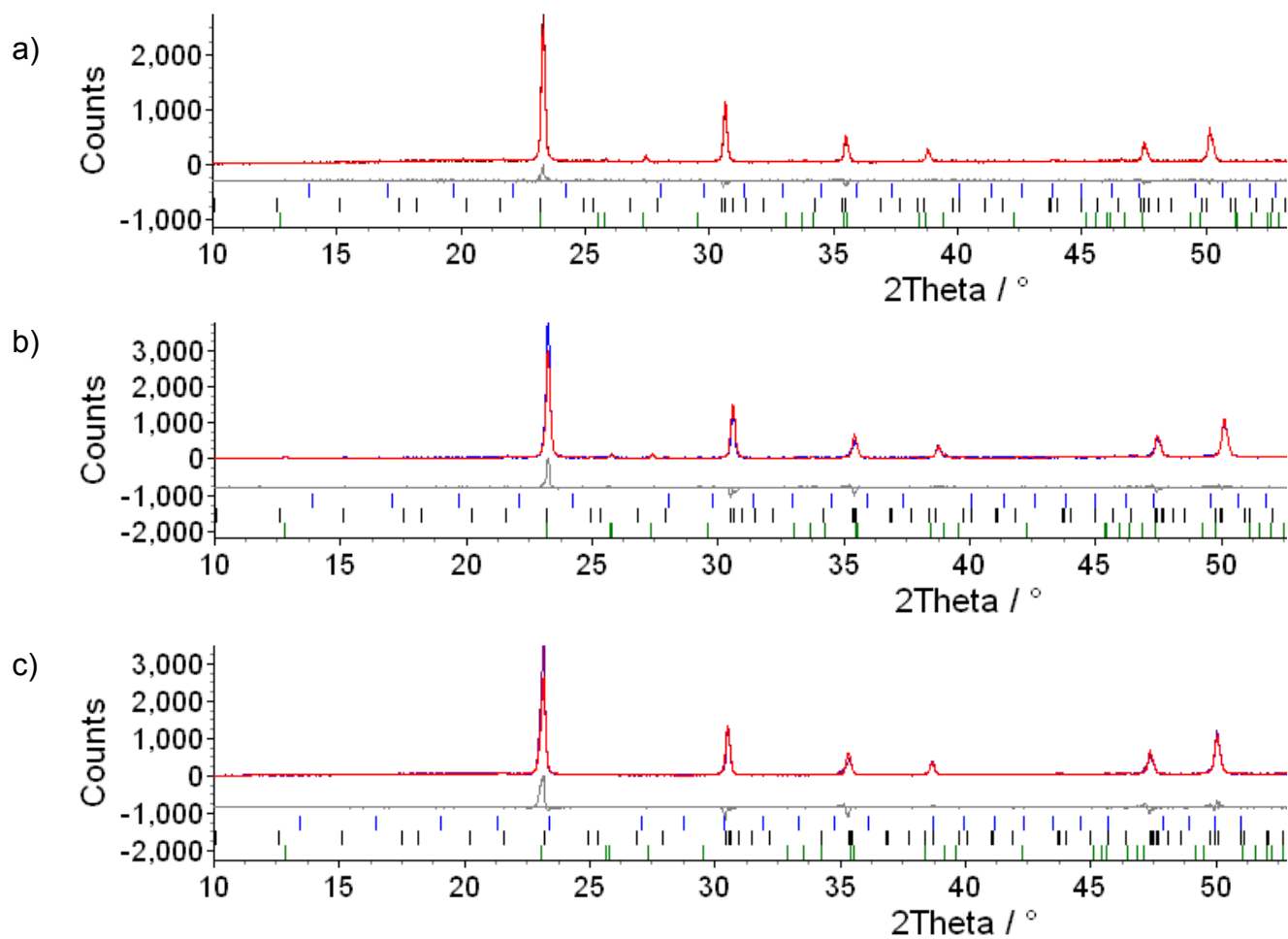
Figure 4.7 Rietveld refinement of XRD data for ZrMo$_2$O$_8$ heated to 823 K *ex-situ* a) JER 100_823 (d5_09491, R$_{wp}$ 12.970 %), b) JER 113_823, (d5_09536, R$_{wp}$ 16.810 %) and c) JER 122_823 (d5_09552, R$_{wp}$ 21.725 %). Bragg peak positions are shown by tick marks for cubic ZrMo$_2$O$_9$ (blue), trigonal ZrMo$_2$O$_8$ (black) and MoO$_3$ (green).
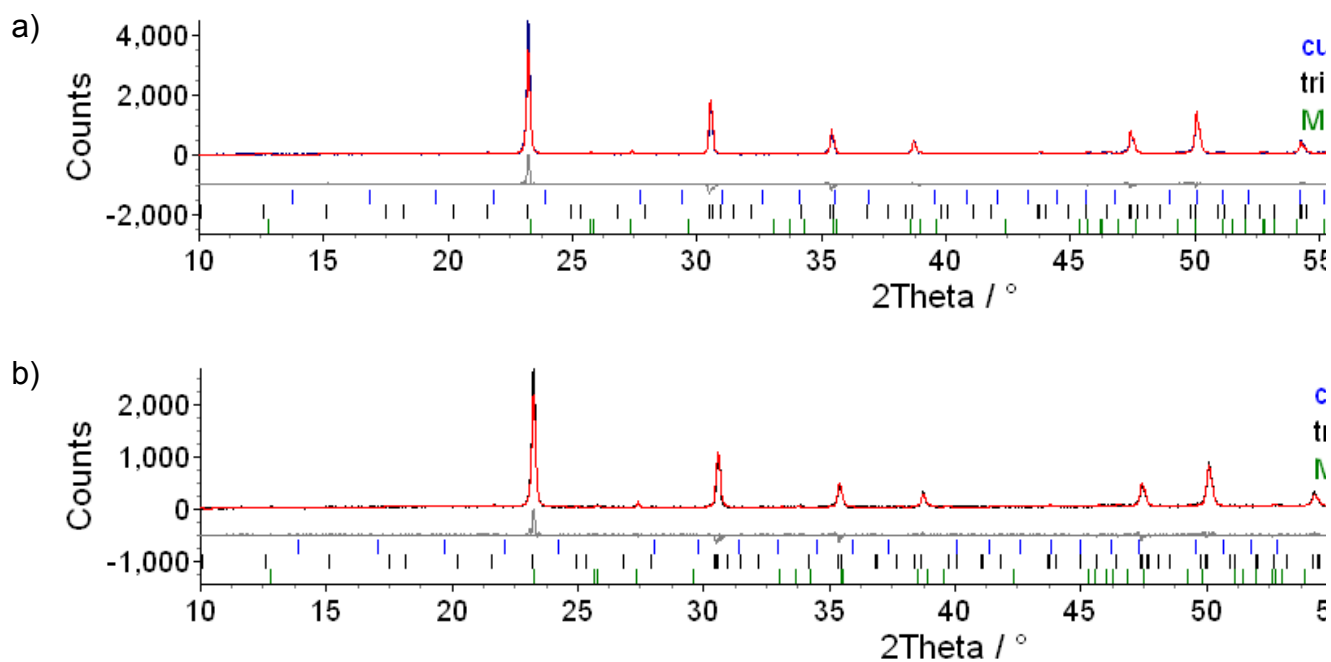
Figure 4.8 Rietveld refinement of XRD data for ZrMo$_2$O$_8$ heated to 923 K *ex-situ* a) JER 100_923 (d5_09533, R$_{wp}$ 16.771 %) and b) JER 113_923, (d5_09535, R$_{wp}$ 11.466 %). Bragg peak positions are shown by tick marks for cubic ZrMo$_2$O$_9$ (blue), trigonal ZrMo$_2$O$_8$ (black) and MoO$_3$ (green).

Ex-situ heating occurred at a heating rate of 10 K^{-1} while *in-situ* heating in the diffractometer occurred at 2 K^{-1}. Heating at the same rate as in HTK 1200 furnace, cubic ZrMo$_2$O$_8$ was formed and PXRD confirmed that cubic ZrMo$_2$O$_8$ was phase pure (Figure 4.9).
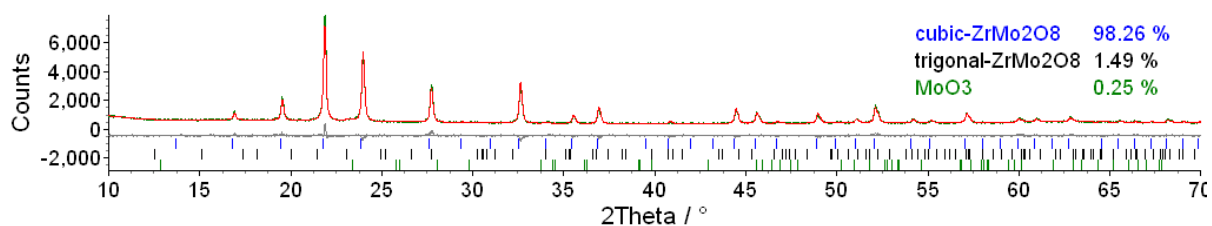

Figure 4.9 Rietveld refinement of XRD data (d7_06729, R$_{wp}$ 5.693 %) of phase pure cubic ZrMo$_2$O$_8$. Bragg peak positions are shown by tick marks for cubic ZrMo$_2$O$_9$ (blue), trigonal ZrMo$_2$O$_8$ (black) and MoO$_3$ (green).

4.2 Particle size from XRD and SEM

Particle sizes of the crystallites were estimated using the method of Balzar *et al.*[55] Initially a highly crystalline sample of CeO_2 was prepared by slowly cooling from 1300 K to room temperature. A high quality data set of this sample was recorded and Rietveld refinement gave an instrumental standard peak-shape (d5_09635). This contribution to the overall peak shape was fixed and convoluted with an additional sample contribution modelled as size broadening. This size contribution was allowed to vary during Rietveld refinement. Diffraction measures volume weighted mean column heights, L_{vol}. This can be converted to the diameter, $r = 4$ L_{vol} / 3, assuming the particles are spherical. The largest size that can be determined by this method using our laboratory system is around 200 nm.

Particle size from PXRD

Table 4.1 shows the phases present at each of the key temperatures and the particle sizes from each *ex-situ* measurement. For samples synthesised from perchloric acid (JER 100 and JER 113), the particle size does not change significantly as the temperature increases. The particle size of the precursor, $ZrMo_2O_7(OH)_2.2H_2O$, differs from VT experiments and ambient temperature XRD, with larger values for the particle size obtained from VT XRD (Figure 4.10 and Figure 4.11). The perchloric acid synthesis samples particle size values are very similar and the e.s.d.s are of the same magnitude. The particle size of hydrochloric acid derived $ZrMo_2O_7(OH)_2.2H_2O$ is much larger (*ca* 120 nm) compared to perchloric acid (*ca* 41 nm). This results in the particle sizes for the subsequent phases of $ZrMo_2O_8$ being much larger. Comparing the variable temperature XRD, this suggests the starting materials and size of precursor particle sizes dictates whether pure cubic-$ZrMo_2O_8$ can be formed. In the case of JER 122, the particle size for LT-$ZrMo_2O_8$ increases significantly as the temperature increases. For cubic-$ZrMo_2O_8$ and trigonal-$ZrMo_2O_8$ the particle size does not change significantly.

Sample		Precursor % / size (nm)	Trigonal % / size (nm)	Cubic % / size (nm)
JER 100	$ZrMo_2O_7(OH)_2.2H_2O$	100/41(0.5)		
HClO$_4$	$ZrMo_2O_8$ 723 K		25 / 73(7)	74 / 65(3)
	$ZrMo_2O_8$ 823 K		88 / 83(3)	
	$ZrMo_2O_8$ 923 K		95 / 134(5)	
JER 113	$ZrMo_2O_7(OH)_2.2H_2O$	100 / 33(1)		
HClO$_4$	$ZrMo_2O_8$ 723 K		21 / 51(5)	88 / 56(2)
	$ZrMo_2O_8$ 823 K		84 / 83(3)	9/3(10)
	$ZrMo_2O_8$ 923 K		95 / 87(3)	
JER 122	$ZrMo_2O_7(OH)_2.2H_2O$	100 / 166 (6)		
HCl	$ZrMo_2O_8$ 723 K		58 / 56(2)	40 / 100(7)
	$ZrMo_2O_8$ 823 K		80 / 87(4)	28 / 3(5)
	$ZrMo_2O_8$ 923 K		100/120 (7)	

Table 4.1 Particle sizes for perchloric acid derived $ZrMo_2O_8$ (JER 100 and JER 113) and hydrochloric acid derived $ZrMo_2O_8$ (JER 122) for each of the phases synthesized from *ex-situ* heating of precursor, $ZrMo_2O_7(OH)_2.2H_2O$ to 723 K, 823 K and 923 K.
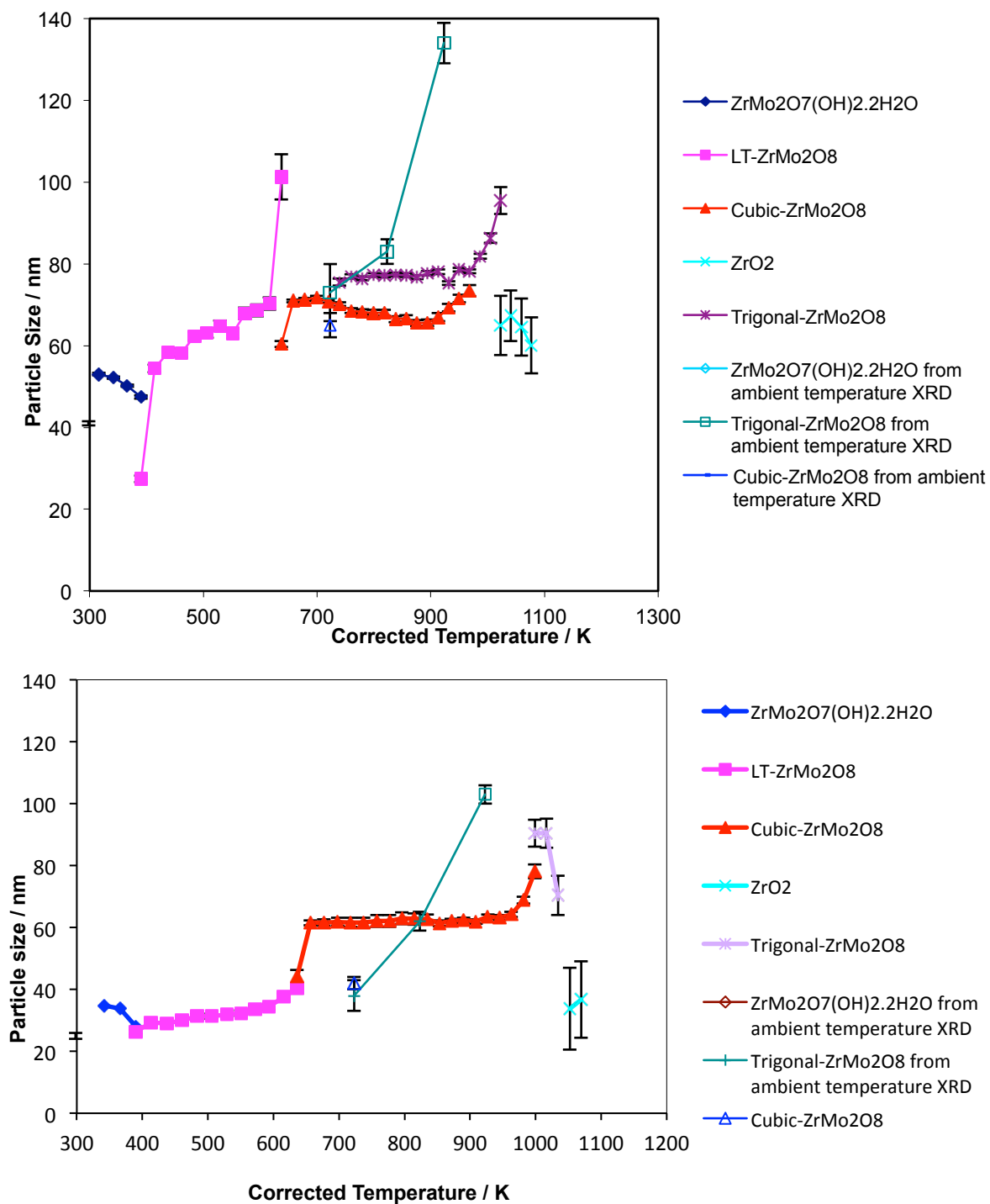
Figure 4.10 Particle size as a function of corrected temperature for perchloric derived ZrMo₂O₈ from VT PXRD and *ex-situ* ambient temperature XRD, JER 100 (top) and JER 113 (bottom).
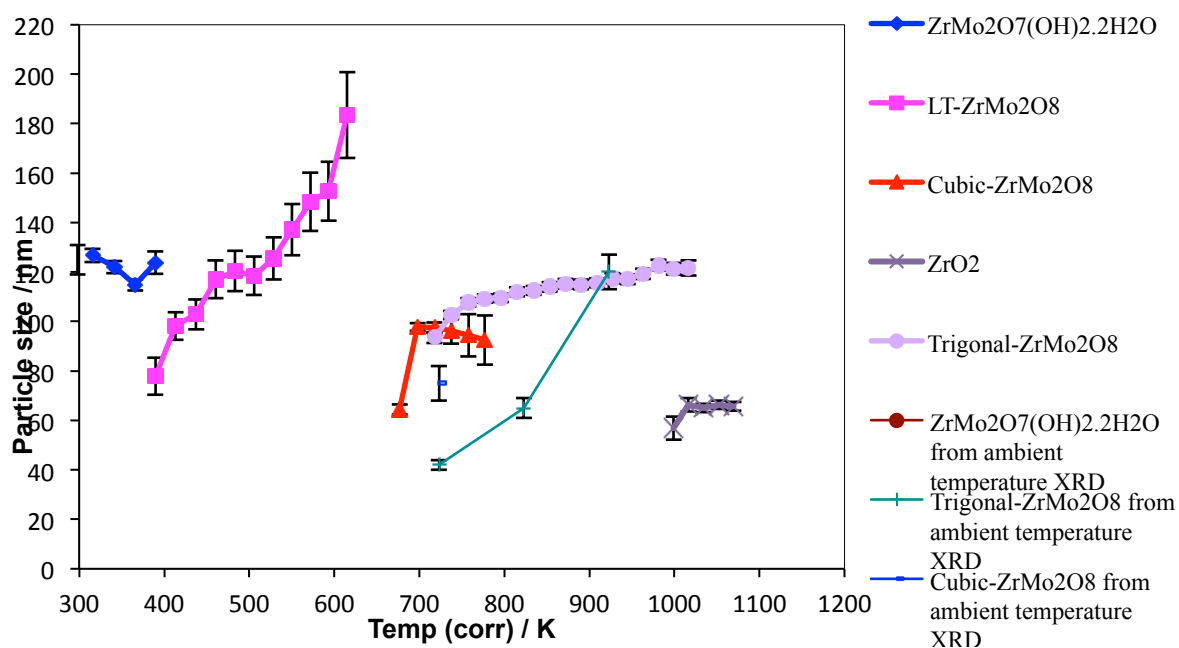
Figure 4.11 Particle size as a function of corrected temperature for chloride derived ZrMo$_2$O$_8$ from VT PXRD and *ex-situ* ambient temperature XRD, JER 122.

Particle size from SEM

Lind *et al.*[56] have previously shown that changing starting reactants from hydrochloric acid to perchloric acid to nitric acid, the particle size and morphology changes, as shown by the SEM images (
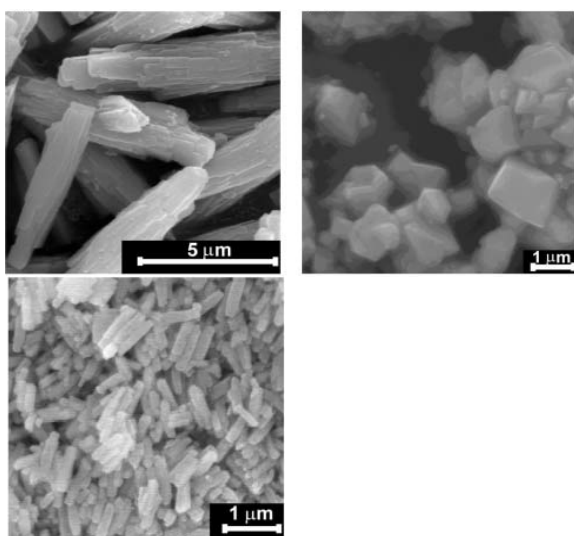
Figure 4.12).

Figure 4.12 Cubic ZrMo$_2$O$_8$ prepared by Lind *et al*. in a chloride environment (top left), in a nitrate environment (top right) and in a perchlorate environment (bottom left).[28]

Figure 4.12 shows the rod-like morphology with agglomeration when hydrochloric acid is used. The particle sizes are between 100 – 500 nm. Using perchloric acid in the synthetic route the resulting crystallites show little agglomeration with particle sizes in the range of 200 – 500 nm. Our X-ray diffraction studies show that the crystallinity of the hydrate is important to favour the formation of cubic $ZrMo_2O_8$. The perchloric acid route results in the smallest crystallites of the hydrate and is thus favoured.

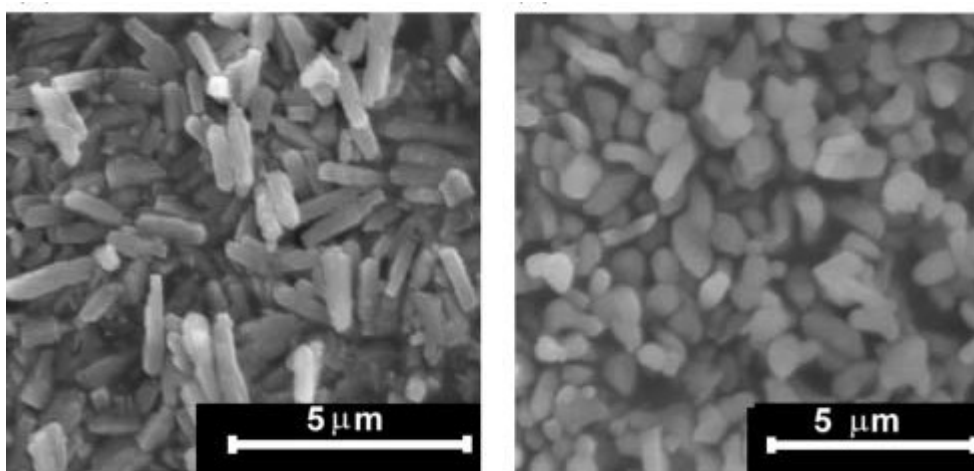**Figure 4.13 SEM images obtained by Lind *et al*. of chloride derived cubic $ZrMO_2O_8$ (left) and perchloric acid derived cubic $ZrMo_2O_8$ (right).[56]**

The SEM images for $ZrMo_2O_7(OH)_2.2H_2O$ for samples JER 100 and JER 113 show the particles to be rod-shaped with ridges on the surface. The square cross section most likely reflects the tetragonal structure. The particle size is *ca* 80 nm in the smallest direction for both samples. Comparing these images to those obtained by Lind *et al*. the precursor in all cases has the same morphology. The particle sizes are also extremely similar.

The morphology of the hydrochloric derived precursor obtained is in agreement with Lind; the particles are cubed-shaped with ridges on the surfaces. The particle size is almost twice that of the perchloric acid derived samples *ca* 150 nm. On heating $ZrMo_2O_7(OH)_2.2H_2O$ through the phase transitions, the bulk of the crystallites remain unchanged. In all the samples a small portion of sample forms very large hexagonal

platelets, presumably due to the trigonal phase, which is surprising as they were not present in previous SEM images reported by Lind *et al* (Figure 4.12 and Figure 4.13). As temperature increases there is evidence of some sintering when trigonal $ZrMo_2O_8$ is the predominant phase, as shown in Figure 4.14 to Figure 4.16. It is possible that individual particles could be agglomerates of much smaller crystalline domains.
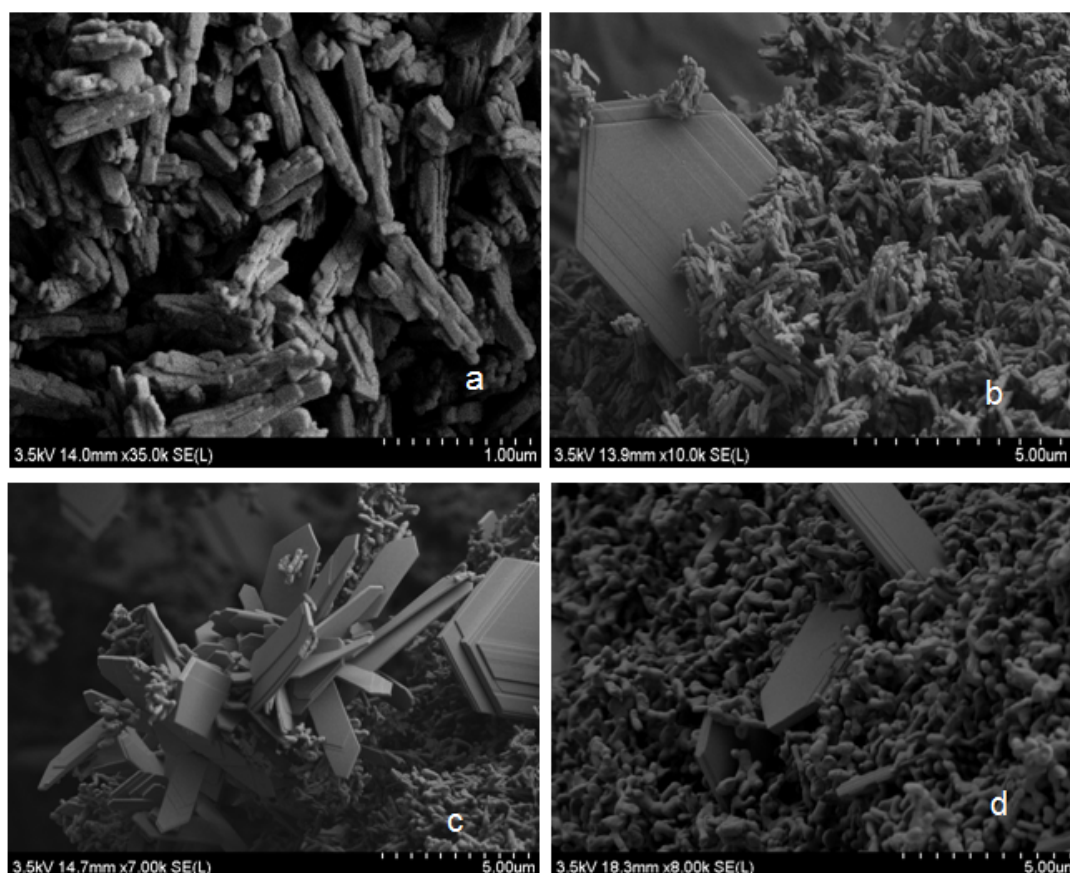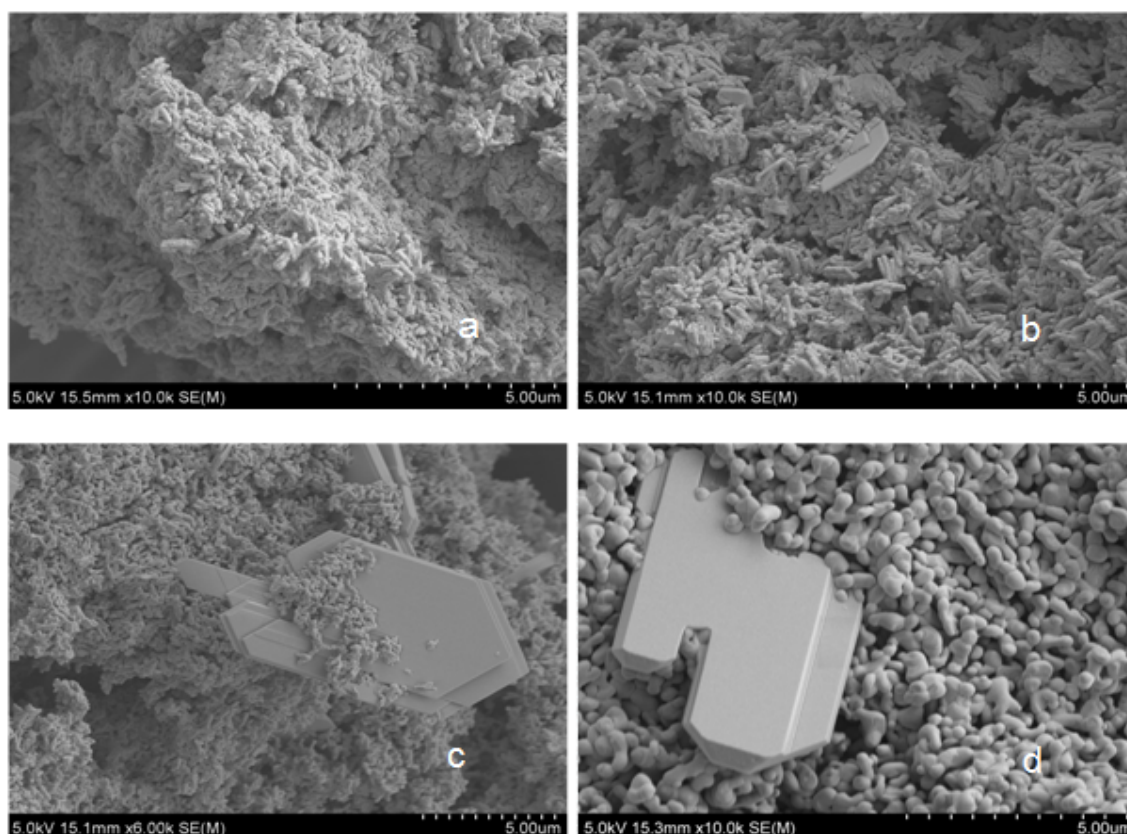

Figure 4.14 SEM images for JER 100 a) $ZrMo_2O_7(OH)_2.2H_2O$, b) a mixture of cubic- and trigonal-$ZrMo_2O_8$ prepared by *ex-situ* heating to 450 $^{\circ}$C, c) trigonal-$ZrMo_2O_8$ prepared by *ex-situ* heating to 550 $^{\circ}$C, d) trigonal-$ZrMo_2O_8$ prepared by *ex-situ* heating to 650 $^{\circ}$C.

Figure 4.15 SEM images for JER 113 a) $ZrMo_2O_7(OH)_2.2H_2O$, b) a mixture of cubic- and trigonal-$ZrMo_2O_8$ prepared by *ex-situ* heating to 450 ^{o}C, c) trigonal-$ZrMo_2O_8$ prepared by *ex-situ* heating to 550 ^{o}C, d) trigonal-$ZrMo_2O_8$ prepared by *ex-situ* heating to 650 ^{o}C.

The estimated particle size for $ZrMo_2O_7(OH)_2.2H_2O$ (JER 100 and JER 113) from the SEM images is *ca* 80 nm, which is approximately twice the diffraction size, although given the approximations involved in the XRD analysis these values can be assumed to be comparable. Alternatively, the differences in the values could be due to the particles becoming single domains once in the cubic phase. As with ambient temperature XRD, the particle sizes for the different phases of $ZrMo_2O_8$ obtained from VT XRD are smaller than the sizes obtained from SEM images. The SEM images show faults and ridges on the surface of the particles; this may cause a smaller particle size to be obtained from XRD data and thus the particle sizes are equivalent. The particle sizes obtained from VT XRD and ambient temperature XRD are comparable.

As with JER 100 and JER 113, the bulk of the particles remain unchanged, but a small proportion form very large platelets of the trigonal-$ZrMo_2O_8$ and sintering occurs at high temperature.
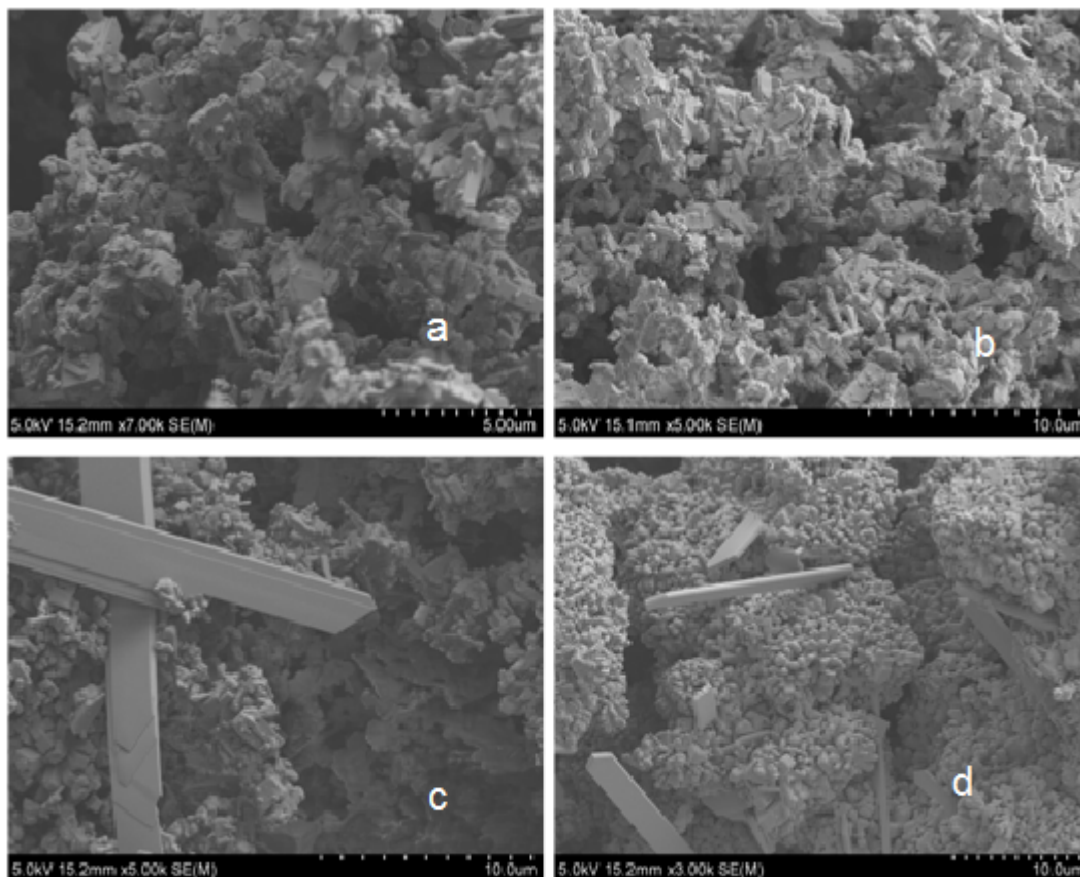

Figure 4.16 SEM images for JER 122 a) $ZrMo_2O_7(OH)_2.2H_2O$, b) a mixture of cubic- and trigonal-$ZrMo_2O_8$ prepared by *ex-situ* heating to 450 ^{o}C, c) trigonal-$ZrMo_2O_8$ prepared by *ex-situ* heating to 550 ^{o}C, d) trigonal-$ZrMo_2O_8$ prepared by *ex-situ* heating to 650 ^{o}C.

4.3 *Ab initio* calculations of $ZrMo_2O_7(OH)_2.2H_2O$, LT, cubic and trigonal $ZrMo_2O_8$

Ab initio calculations were performed using the CASTEP programme, as discussed in detail in Chapter 2, on precursor, LT, cubic and trigonal $ZrMo_2O_8$. Using the geometry optimised co-ordinates, the NMR parameters were calculated using CASTEP[57] and the spectra for the central transition were simulated using the programme pNMRsim[58] assuming uniform excitation (i.e. an ideal 90° pulse). To verify whether the optimised structures for each of the phases were chemically

viable, bond valence sums were calculated and these results tabulated. If the bond valence values were within 5-10 % of the expected values of +4 and +6 for Zr and Mo respectively, the optimised structure was assumed to be reasonable and was then used to calculate the NMR parameters. If the values were inconsistent, changes to the geometry optimisation calculation parameters and subsequent recalculation of the optimised structure was performed. This was particularly true for precursor, $ZrMo_2O_7(OH)_2.2H_2O$ calculations.

To reference the calculated shielding (σ) values to the experimental *chemical shifts* (δ), the sign of the calculated shieldings were reversed and referenced to the weighted mean of trigonal $ZrMo_2O_8$ experimental chemical shifts (607.5 ppm).

$ZrMo_2O_7(OH)_2.2H_2O$

The structure of the precursor, $ZrMo_2O_7(OH)_2.2H_2O$, was obtained by Clearfield and Blessing[53] using single crystal X-ray diffraction, although the positions of the hydrogen atoms were unknown at the time as this predated neutron diffraction studies. Allen[3] located the hydrogen atoms using neutron diffraction data and a combination of Clearfield and Blessing's[53] and Allen's coordinates were used (Table 4.2). The lattice parameters were *a* = 11.45 Å and *c* = 12.47 in space group *I41cd*.

	x	*y*	*z*
Zr	0	0	0
Mo (1)	0.02971 (15)	0.16780 (18)	0.23482 (20)
Mo (11)	-0.01187 (5)	0.15980 (2)	0.23124 (22)
O (1)	0.17450	0.16591	0.24661
D (11)	0.23440	0.10313	0.24014
D (12)	0.22074	0.23922	0.25537
O (2)	0.82641	0.16284	0.22362
D (21)	0.80047	0.11977	0.28884
D (22)	0.78808	0.24079	0.22969
O (3)	0.17253 (8)	0.99669 (15)	0.99352 (10)
O (4)	-0.01224 (8)	0.11942 (6)	0.86490 (9)
O (5)	0.00140	0.16796	0.06447
O (51)	-0.05811	0.22802	0.04515
O (52)	0.04366	0.24088	0.04395
O (6)	0	0	0.17930 (14)

Table 4.2 Refined positional coordinates obtained from a combination of X-ray and neutron diffraction data (Clearfield and Blessing and Allen). E.S.D. values are not available for atoms modelledas rigid bodies, *i.e.* water bearing and hydroxyl oxygen and corresponding deuterium.

The geometry optimisation calculations had difficulties and would not converge after 100 iterations. This difficulty could be due to the presence of a framework as well as molecules of water (water of condensation). In order to try and overcome this problem, step wise geometry optimisation of the framework and water molecules were performed. Using the starting structure (as listed in Table 4.2) a geometry optimisation calculation where only the hydrogen atomic positions were optimised was performed. This structure was then used as the starting structure for another geometry optimisation calculation in which the oxygen atomic positions were fixed and all the other atomic positions (including hydrogen positions) were optimised. Only very subtle changes were seen in the atomic coordinates after this geometry optimisation calculation. The resulting optimised structure was used for another geometry optimisation calculation in which all the atomic positions were unfixed and

the calculation was allowed to optimise. However, the resulting structure was chemically unreasonable.

It is likely that the presence of both molecules and framework structure makes geometry optimisation calculations for this phase extremely difficult. Given the limited interest of the precursor material no further CASTEP[57] calculations on this phase were attempted.

LT ZrMo$_2$O$_8$

The structure of LT ZrMo$_2$O$_8$ can be described by a 3D array of corner-sharing ZrO$_6$ octahedra and MoO$_4$ tetrahedra with a singly coordinated oxygen atom. The LT structure is very similar to that of cubic ZrMo$_2$O$_8$ which exhibits NTE and hence it is not surprising that LT ZrMo$_2$O$_8$ also exhibits this property. The starting unit cell has 22 atoms and the CASTEP geometry optimisation calculation used the fractional coordinates as published by Evans *et al.*,[25] obtained from HRPD. Table 4.3 lists the bond lengths and bond valence values for Zr and Mo atoms. The optimised structure was chemically reasonable and the NMR parameters were calculated from this structure.
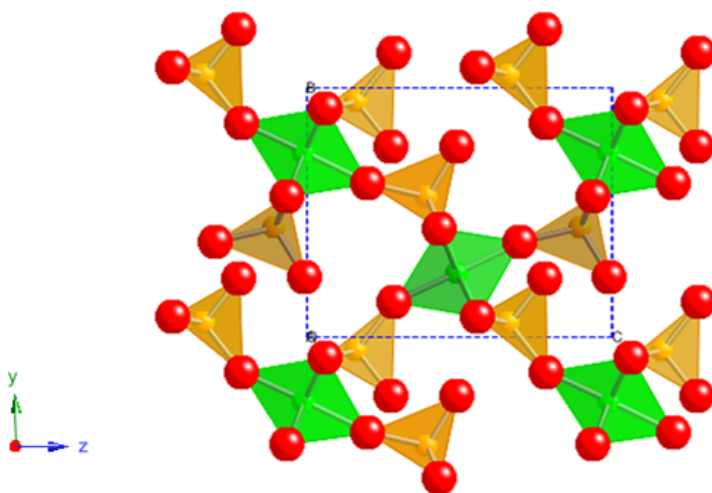

Figure 4.17 Geometry optimised structure of LT ZrMo$_2$O$_8$ from CASTEP calculation. Oxygen atoms (red), ZrO$_6$ octahedra (green) and MoO$_4$ (orange).

M	A	M-A (Å) Unoptimised / (number of bonds)	Total bond valence	M-A (Å) Optimised / (number of bonds	Total bond Valence
Zr	**O**	2.0524 / 2		2.0401 / 1	
	O	2.0817 / 1		2.0941 / 1	
	O	2.1093 / 2		2.1050 / 2	
	O	2.1498 / 1	3.95	2.1302 / 2	3.86
Mo	**O**	1.4652 / 1		1.7125 / 1	
	O	1.8742 / 2		1.7865 / 1	
	O	2.5310 / 1	5.67	1.7993 / 2	5.75
Mo	**O**	1.5114 / 1		1.6961 / 1	
	O	1.2092 / 1		1.8128 / 1	
	O	2.0248 / 2		1.8149 / 2	
	O	2.3209 / 1	11.28	2.6303 / 1	5.76

Table 4.3 Comparison of bond lengths between Zr and O and Mo and O in LT ZrMo$_2$O$_8$ in unoptimised and optimized structures. The total bond valence for each metal is shown.

Table 4.6 shows the raw shieldings and electric field gradient (EFG) tensors, from CASTEP, for the unique sites of LT ZrMo$_2$O$_8$. The anisotropic chemical shielding for Mo (2) is unusually high with a value of -3858.6 ppm and the values for oxygen are also higher than expected. The CASTEP output files contained unexpected warnings about the system being metallic, with non-zero electron density in what should be unfilled bands above the band gap. In subsequent calculations, the system was forced to be an insulator (fix_occupancy : true in the .param file). A comparison of the parameters calculated with and without the electron occupancy fixed, are listed in Table 4.4. Forcing the system to be an insulator changes the calculation results significantly. Given the clearly insulating nature of the materials, this behaviour is unexpected and has been taken up with Jonathan Yates, one of the developers of CASTEP, for further investigation.